# ATLAS NOTE

ATLAS-CONF-2013-051

May 17, 2013


# Search for anomalous production of events with same-sign dileptons and $b$ jets in 14.3 fb$^{-1}$ of pp collisions at $\sqrt{s} = 8$ TeV with the ATLAS detector

The ATLAS Collaboration

**Abstract**

A search is presented for exotic processes that result in final states containing jets including at least one $b$ jet, sizable missing transverse momentum, and a pair of leptons with the same electric charge. There are several models that predict an enhanced rate of production of such events beyond the expectations of the Standard Model (SM); the ones considered in this note are pair production of chiral $b'$ quarks, pair production of vector-like quarks, enhanced four top quark production and production of two positively-charged top quarks. Using a sample of 14.3 fb$^{-1}$ of $pp$ collisions at $\sqrt{s} = 8$ TeV recorded by the ATLAS detector at the Large Hadron Collider, with selection criteria optimised for each signal, no significant excess of events over the background expectation is observed. This observation is interpreted as constraining the signal hypotheses, and it is found at 95% confidence level that: the mass of the $b'$, assuming 100% branching fraction to $Wt$, must be $> 0.72$ TeV; the mass of a vector-like $B$ ($T$) quark, assuming branching ratios to $W$, $Z$, and $H$ decay modes consistent with the $B$ or $T$ being a singlet, must be $> 0.59$ (0.54) TeV; the four top production cross section must be $< 85$ fb in the SM and $< 59$ fb for production via a contact interaction; the mass of an sgluon must be $> 0.80$ TeV; in the context of models with two universal extra dimensions the inverse size of the extra dimensions must be $> 0.90$ TeV; and the cross section for production of two positively-charged top quarks must be $< 210$ fb.



ATLAS-CONF-2013-051
17/05/2013

# 1 Introduction

The Standard Model (SM) has been repeatedly confirmed experimentally; nonetheless there appears to be a need for physics beyond the SM at about the weak scale, with additional features that explain the presence of dark matter in the universe, and provide a mechanism to naturally stabilize the Higgs boson mass at its observed value of $\approx 125$ GeV [1, 2]. This note reports on a search for new physics resulting in isolated high-$p_T$ lepton pairs with the same electric charge and $b$ jets. This is a promising search channel since the SM yields of such events are small, and several types of new physics may contribute.

Among the models that predict enhanced same-sign lepton production are those that postulate the existence of a fourth generation of chiral quarks, the existence of vector-like quarks, an enhancement of the four top quark production cross section, or production of two positively-charged top quarks. We use a common data sample to search for each of these signatures, and optimise the event selection criteria for each signal model.

A fourth generation of SM quarks includes a charge $-1/3$ quark, called the $b'$. Under the assumption that the $b'$ decays predominantly to $Wt$, $b'$ pair production results in four $W$ bosons in the final state. If two of the $W$ bosons with the same electric charge decay leptonically, there will be a same-sign lepton pair in the final state. The existence of additional quark generations greatly enhances the Higgs boson production cross section, so if the new boson observed at the LHC is a manifestation of a minimal Higgs sector, additional quark generations are ruled out. However, a more complex Higgs sector, as in Two-Higgs-Doublet models [3], allows a fourth generation.

Several extensions to the SM that regulate the Higgs boson mass in a natural way require the existence of vector-like quarks (VLQ) [4–22], where "vector-like" means that the left- and right-handed components transform identically under the $SU(2)_L$ weak isospin gauge symmetry. Since quarks with this structure do not require a Yukawa coupling to the Higgs field to attain mass, their existence would not enhance the Higgs boson production cross section, and thus the motivation persists for a direct search. There are several possible varieties of VLQ; those having the same electric charge as the SM $b$ and $t$ quarks are called $B$ and $T$. VLQ may exist as either isospin singlets, doublets, or triplets. Arguments based on naturalness suggest that VLQ may not interact strongly with light SM quarks [23, 24]. Thus it is assumed for this analysis that VLQ decay predominantly to third-generation SM quarks. Both charged- and neutral-current decays may occur, providing many paths for same-sign lepton production for events with VLQ. For example, the decays $B \to Wt$, $T \to Zt$, and $T \to Ht$ can all lead to same-sign lepton pairs (depending on the decays of the $W$, $Z$, and $H$ bosons) in association with $b$ jets and missing transverse momentum ($E_{\mathrm{T}}^{\mathrm{miss}}$) when VLQ are pair-produced. The branching fractions to each allowed final state are model-dependent; as a reference we will use the branching ratios naturally occurring in models where the $B$ and $T$ exist as singlets or doublets [25]. These branching fractions vary with the mass of the VLQ, and values for masses near the limit of our sensitivity are given in Table 1. Since the pair production of heavy quarks is mediated by the strong interaction, the cross section is identical for $b'$ and vector-like quarks of a given mass. The NNLO cross sections from HATHOR [26] are used in this note.

Same-sign lepton pairs may also arise from the non-resonant production of four top quarks ($t\bar{t}t\bar{t}$). The SM rate for this production is small ($\approx 1$ fb [27, 28]), but there are several new physics models that can enhance the rate. These can generically be described in terms of a four-fermion contact interaction with coupling strength $C/\Lambda^2$, where $C$ is the coupling constant and $\Lambda$ is the scale of the new physics [29]:

$$\mathcal{L} = \mathcal{L}_{\mathrm{SM}} + \frac{C}{\Lambda^2}\left(\bar{t_R}\gamma^\mu t_R\right)\left(\bar{t_R}\gamma_\mu t_R\right). \tag{1}$$

Two specific models are also considered. The first is sgluon pair production, where sgluons are color-adjoint scalars that appear in several extensions to the SM [30–35]. If the sgluon mass is above the top quark pair production threshold, the dominant decay is to $t\bar{t}$, resulting in four top quarks in the final state ($t\bar{t}t\bar{t}$). The cross-sections considered in this paper are rescaled to NLO [36]. The second

Table 1: VLQ branching fractions (in percent) for masses near the limit of our sensitivity, assuming the singlet and doublet models of [25].

| | $B$ | | | $T$ | | |
|---|---|---|---|---|---|---|
| Mass (model) | $Wt$ | $Zb$ | $Hb$ | $Wb$ | $Zt$ | $Ht$ |
| 0.50 TeV (singlet) | 42 | 31 | 27 | 50 | 17 | 33 |
| 0.50 TeV (doublet) | 100 | 0 | 0 | 0 | 34 | 66 |
| 0.55 TeV (singlet) | 43 | 30 | 27 | 49 | 18 | 32 |
| 0.55 TeV (doublet) | 100 | 0 | 0 | 0 | 37 | 63 |
| 0.60 TeV (singlet) | 44 | 29 | 26 | 49 | 19 | 31 |
| 0.60 TeV (doublet) | 100 | 0 | 0 | 0 | 38 | 62 |
| 0.65 TeV (singlet) | 45 | 29 | 26 | 49 | 20 | 30 |
| 0.65 TeV (doublet) | 100 | 0 | 0 | 0 | 40 | 60 |

model is one with two universal extra dimensions under the real projective plane geometry (2UED/RPP) [37]. The compactification of the extra dimensions leads to discretisation of the momenta along their directions, which is quantified here as a Kaluza-Klein mass ($m_{KK} \equiv \frac{1}{R_4}$, where $R_4$ is related to the size of the first extra dimension[1]). This model predicts the pair production of Kaluza-Klein excitations of the photon with mass $\sqrt{2}m_{KK}$, each of them decaying to $t\bar{t}$, with a branching fraction assumed to be 100%. Cosmological observations constrain $m_{KK}$ to lie approximately between 600 GeV and 1000 GeV [38]. The search for four top quark production reported here is an extension of an analysis done with the 2011 ATLAS data set, which placed the first constraints on four top quark production [39].

Production of two positively-charged top quarks via $uu \to tt$ can also result in an excess of same-sign lepton pairs. This process may be mediated via s- or t-channel exchange of a heavy particle [40,41]. If the mass of the mediating particle is much greater than the electroweak symmetry breaking scale, an effective four-fermion contact interaction can describe the process, with separate operators for the different initial-state chiralities, as defined in Eq. 9.1 of [42].

Previous searches at ATLAS [39], using 4.7 fb$^{-1}$ of data at $\sqrt{s} = 7$ TeV, and CMS [43], using 19.7 fb$^{-1}$ at $\sqrt{s} = 8$ TeV, did not observe a significant excess of same-sign dilepton production. The ATLAS result ruled out a $b'$ quark with mass less than 0.67 TeV, and set an upper limit on the four top quark production cross section of 0.06 pb, both at 95% C.L. The CMS result was not interpreted in the context of the models considered here. The results reported in this note extend the previous ATLAS search by using a larger data sample that was recorded at $\sqrt{s} = 8$ TeV.

## 2 Data and Monte Carlo Simulation

The data used were recorded by the ATLAS detector [44] at the LHC $pp$ collider operating at $\sqrt{s} = 8$ TeV between April and October 2012, and correspond to an integrated luminosity of 14.3 fb$^{-1}$. The ATLAS detector consists of an inner tracking system surrounded by a superconducting solenoid that provides a 2 T magnetic field, electromagnetic (EM) and hadronic calorimeters, and a muon spectrometer. The inner detector provides tracking information from pixel and silicon microstrip detectors within pseudorapidity[2]

[1] In the model tested here, both extra dimensions have the same size, i.e. $R_4 = R_5$.

[2] ATLAS uses a right-handed coordinate system with its origin at the nominal interaction point (IP) in the centre of the detector and the $z$ axis coinciding with the axis of the beam pipe. The $x$ axis points from the IP to the centre of the LHC ring, and the $y$ axis points upward. Cylindrical coordinates ($r$,$\phi$) are used in the transverse plane, $\phi$ being the azimuthal angle around the beam pipe. The pseudorapidity is defined in terms of the polar angle $\theta$ as $\eta = \ln\tan(\frac{\theta}{2})$. For the purpose of the fiducial selection, this is calculated relative to the geometric centre of the detector; otherwise, it is relative to the reconstructed primary

$|\eta| < 2.5$, and from a transition radiation tracker that covers $|\eta| < 2.0$. The EM sampling calorimeter uses lead and liquid argon (LAr), and is divided into a barrel region that covers $|\eta| < 1.475$ and end-cap regions that cover $1.375 < |\eta| < 3.2$. The hadronic calorimeter consists of either LAr or scintillating tile as the active medium, and steel, copper, or tungsten as the absorber, and covers $|\eta| < 4.9$. The muon spectrometer covers $|\eta| < 2.7$, and uses multiple layers of high-precision tracking chambers to measure the deflection of muons tracks as they traverse a toroidal field of 0.5 (1.0) T in the central (end-cap) regions of ATLAS.

Signal and some background sources were modelled using Monte Carlo (MC) simulations. The remaining background sources are determined from the data, as described in Section 4. Pair production of $b'$ events was modelled with the PYTHIA [45] generator (v6.425), for $b'$ masses ranging from 400 to 1000 GeV. VLQ production was modelled using the PROTOS [25] v2.2 generator, with PYTHIA used to model extra gluon emission and hadronization. Production of two positively-charged top quarks was also modelled using PROTOS [42] and PYTHIA, with three different chirality configurations of the contact interaction operator. Production of four top quarks was modelled under four scenarios: *i*) standard model production, *ii*) production arising from a contact interaction, *iii*) production as a result of sgluon pair production, and *iv*) production arising from the presence of two universal extra dimensions. The sgluon case was generated with PYTHIA v8.17; the other three models were generated with MADGRAPH [46] v5.1 followed by PYTHIA v6.4. Backgrounds from $t\bar{t}+W/Z/W^+W^-$ and $W^\pm W^\pm jj$ production were modelled with MADGRAPH followed by PYTHIA v6.4, while $WZ$ and $ZZ$ plus jet production was modelled using SHERPA [47] v1.4.0. A variable number of additional $pp$ interactions were overlaid on simulated events to model the effect of multiple collisions during a single bunch crossing, and also the effect of the detector response to collisions from bunch crossings before or after the one containing the hard interaction. Events were then weighted to reproduce the distribution of the number of collisions per bunch crossing observed in data. The detector response was modelled using either a GEANT4 [48, 49] simulation or a faster simulation that combined GEANT simulation of the inner tracker and of muons with a fast simulation of shower development in the calorimeter. Some samples were generated both with GEANT4 and the fast simulation, to allow direct comparison between the two, and agreement was found within the systematic uncertainty assigned to the efficiency estimate. In all cases the simulated events were reconstructed using the same algorithms that were applied to the collision data.

## 3 Event selection

The final state considered in this search requires the presence of exactly two leptons[3] in the event, both with the same electric charge. In addition, two or more jets are required, at least one of which is consistent with being a $b$ jet, and sizable $E_{\mathrm{T}}^{\mathrm{miss}}$. The criteria used for each of these objects are given below.

Each event is required to have at least one reconstructed vertex, which must be formed from at least five tracks. If there are multiple vertices reconstructed, the vertex with the largest sum of the squared transverse momenta of its associated tracks is taken as the primary vertex. In addition, events are required to pass either an electron trigger (where the triggers chosen require either an isolated electron with $p_{\mathrm{T}} > 24$ GeV or an electron with $p_{\mathrm{T}} > 60$ GeV with no isolation requirement) or a muon trigger (where the triggers chosen require either an isolated muon with $p_{\mathrm{T}} > 24$ GeV or a muon with $p_{\mathrm{T}} > 36$ GeV with no isolation requirement). Jets are reconstructed using an anti-$k_t$ algorithm [50–52] with distance parameter 0.4. If one or more jets are within $\Delta R \equiv \sqrt{\Delta\eta^2 + \Delta\phi^2} = 0.2$ of an electron, the jet closest to the electron is discarded (i.e. the calorimeter cluster is treated as an electron rather than a jet). To suppress jets that do not originate from the primary event vertex, the jet vertex fraction (JVF) is defined

vertex of each event.

[3]Only electrons and muons are considered in the search. Tau leptons are not explicitly reconstructed, but electrons and muons from tau decay may enter the selected samples.

by considering all tracks within the jet, and finding the fraction of the summed $p_{\mathrm{T}}$ of these tracks that comes from tracks that originate from the primary vertex. Jets are required to have JVF $> 0.5$, $p_{\mathrm{T}} > 25$ GeV (after energy calibration [53]) and $|\eta| < 2.5$.

A multivariate algorithm [54] is used to test the consistency of each jet with arising from a $b$ quark, based on the properties of the tracks associated with the jet. A requirement is placed on the output of the discriminant such that $\approx 70\%$ of $b$-quark jets and $\approx 1\%$ of light quark or gluon jets are expected to pass. All jets that meet this criterion are called '$b$-tagged' jets.

Electrons [55] are identified by requiring a track to match an electromagnetic calorimeter cluster, subject to several criteria on the shape of the shower and the consistency between the shower and track. The selection requirements are varied with the $\eta$ and $p_{\mathrm{T}}$ of the electron candidate to optimise the signal efficiency and background rejection. The track is required to be consistent within 2 mm in $z$ with the reconstructed primary vertex of the event. A hit in the innermost layer of the inner detector is required, for active modules, to reject photon conversions. Electron clusters are required to have $E_{\mathrm{T}} > 25$ GeV and $|\eta| < 2.47$, with the region $1.37 < |\eta| < 1.52$ excluded. The candidate is required to be isolated from additional calorimeter energy within a cone of $\Delta R = 0.2$ and from additional tracks within a cone of $\Delta R = 0.4$, with the amount of additional energy or track $p_{\mathrm{T}}$ allowed chosen such that the efficiency for electrons from $Z$ boson decay to satisfy each isolation requirement is 90% in MC simulated samples. In addition, electrons are required to be separated from any jet by at least $\Delta R = 0.4$.

Muons [56–58] are identified from hits in the muon system matched to a central track, where the track must be within 2 mm in $z$ of the primary vertex. Requirements are placed on the number of hits in various layers of the muon system, and on the maximum number of layers where hits are missing. Muon pairs that are consistent with the passage of a cosmic ray are discarded. To suppress muons arising from heavy quark decays, the muon candidates are required to be isolated from other central track activity within a cone with radius that decreases with increasing muon $p_{\mathrm{T}}$ [59]: $\Delta R = 0.4/(p_{\mathrm{T}}/10\ \mathrm{GeV})$. The summed $p_{\mathrm{T}}$ of all tracks (other than the muon track) in that cone is required to be less than 5% of the muon $p_{\mathrm{T}}$. Muons are also required to be separated from any jet by $\Delta R = 0.4$, and to have $p_{\mathrm{T}} > 25$ GeV and $|\eta| < 2.5$. Events with a muon within $\Delta R = 0.2$ of any electron are rejected.

The missing transverse momentum is calculated as the opposite of the vector $E_{\mathrm{T}}$ sum from all calorimeter cells, corrected for the energy carried away by identified muons. Energy scale corrections applied to electrons and jets are also propagated to $E_{\mathrm{T}}^{\mathrm{miss}}$. Events are required to have $E_{\mathrm{T}}^{\mathrm{miss}} > 40$ GeV.

Events are also required to be from a run where the detector performance is known to be good. Depending on the flavour of the leptons the event is identified as an $ee$, $e\mu$, or $\mu\mu$ candidate. If the same-sign leptons are of the same flavour, their invariant mass $m_{\ell\ell}$ is required to be $> 15$ GeV and to satisfy $|m_{\ell\ell} - m_Z| > 10$ GeV. This rejects events from a resonance where the charge of one lepton is misidentified. Finally, the scalar sum of all jet and lepton $p_{\mathrm{T}}$'s ($H_{\mathrm{T}}$), is required to be $> 550$ GeV. These basic selection criteria are applied to all searches; some of them are tightened when optimising the selection for each signal model (see Section 6). The distributions of the most relevant kinematic variables for background and for two signals are shown for the $e\mu$ channel in Fig. 1, and for the $ee$ and $\mu\mu$ channel in the appendix (Figs. 11-12).

# 4 Background Estimation

Backgrounds arise from two distinct sources: SM processes that result in the same final-state objects as the signal, and instrumental backgrounds where objects are misidentified or misreconstructed such that they appear to have the same final state. The former category includes $WZ$ and $ZZ$ production in association with a heavy flavour jet, $W^{\pm}W^{\pm}jj$ production, $t\bar{t}+W$ production, $t\bar{t}+Z$ production, and $t\bar{t}+W^{+}W^{-}$ production. All of these processes have small cross sections, and the expected yields from them are computed using simulation.

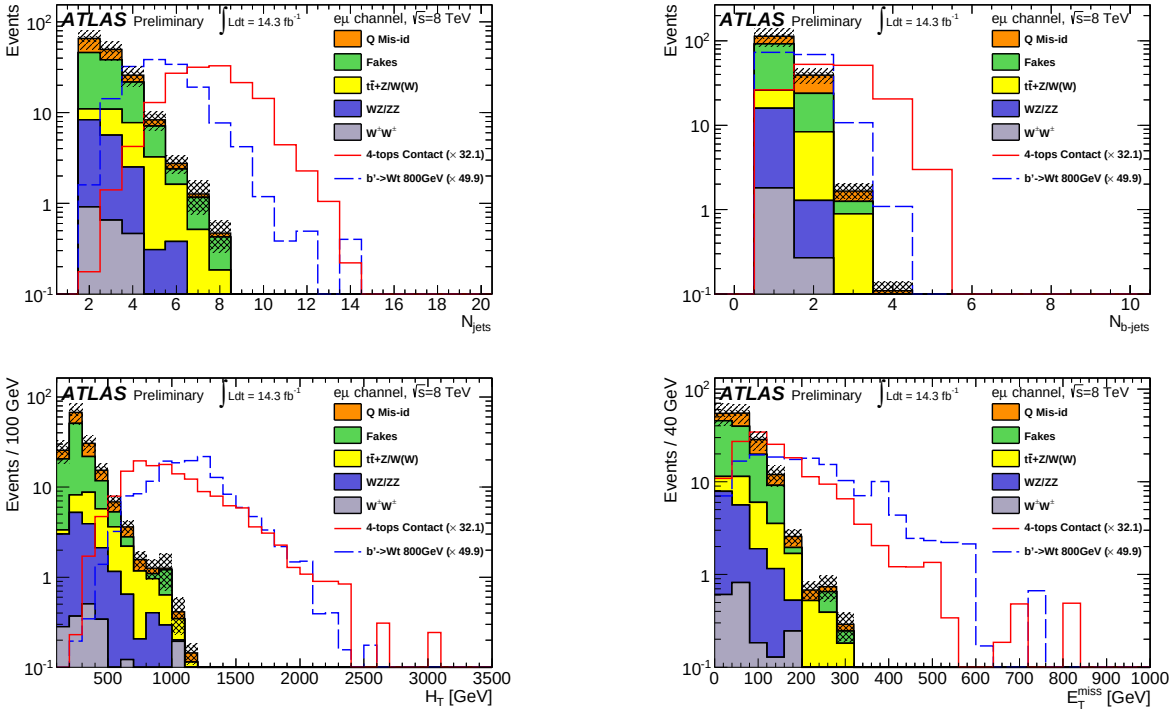


Figure 1: Distributions of discriminant variables in the $e\mu$ channel, after the standard object selection and with the requirement that $E_{\mathrm{T}}^{\mathrm{miss}} > 40$ GeV. The cross section for each signal model is scaled up so that the signal integrals are all equal to the background integral. The assumed strength of the contact interaction is $C/\Lambda^2 = -4\pi$ TeV$^{-2}$. The background histograms are stacked to show the total expected background, while each signal histogram is independent of the others. The uncertainties on the background shown here consist of the production cross section uncertainty for the backgrounds modelled with Monte Carlo simulation, and a 30% uncertainty for instrumental backgrounds (see Section 5).

Instrumental backgrounds can be further separated into two categories: *i*) events that contain two leptons of opposite charge, where one of the charges is mismeasured and *ii*) events where one or more jets are misidentified as leptons. To estimate the number of events with misidentified leptons, we begin by relaxing the lepton identification criteria to form a *loose* sample. Only events with exactly two leptons are retained in the loose sample. Single lepton events were used to measure the probabilities $r$ and $f$ for real and fake leptons selected using the loose criteria to also satisfy the standard (or *tight*) criteria. For electrons, $r$ was measured using events with $E_{\mathrm{T}}^{\mathrm{miss}} > 150$ GeV, and $f$ was measured using events with $E_{\mathrm{T}}^{\mathrm{miss}} < 20$ GeV and $E_{\mathrm{T}}^{\mathrm{miss}} + m_T(W) < 60$ GeV. For muons, $r$ was measured using events with $m_T(W) > 100$ GeV, and $f$ was measured using events where the impact parameter of the muon with respect to the primary vertex was more than five standard deviations from zero. These probabilities are parameterised with respect to properties of the leptons (e.g. $\eta$ and $p_{\mathrm{T}}$) and of the event (e.g. $E_{\mathrm{T}}^{\mathrm{miss}}$ and number of $b$-tagged jets). The estimated number of events with one or more misidentified leptons entering the selected sample is then:

$$
\begin{aligned}
N^{\mathrm{tt}}_{\mathrm{fake}} &= N^{tt}_{\mathrm{rf}} + N^{\mathrm{tt}}_{\mathrm{fr}} + N^{\mathrm{tt}}_{\mathrm{ff}} \\
&= r_1 f_2 N^{\mathrm{ll}}_{\mathrm{rf}} + f_1 r_2 N^{\mathrm{ll}}_{\mathrm{fr}} + f_1 f_2 N^{\mathrm{ll}}_{\mathrm{ff}} \\
&= \alpha r_1 f_2 \left[(f_1 - 1)(1 - r_2)N^{\mathrm{tt}} + (1 - f_1)r_2 N^{\mathrm{tl}} + f_1(1 - r_2)N^{\mathrm{lt}} - f_1 r_2 N^{\mathrm{ll}}\right] \\
&\quad + \alpha f_1 r_2 \left[(r_1 - 1)(1 - f_2)N^{\mathrm{tt}} + (1 - r_1) f_2 N^{\mathrm{tl}} + r_1(1 - f_2)N^{\mathrm{lt}} - r_1 f_2 N^{\mathrm{ll}}\right] \\
&\quad + \alpha f_1 f_1 \left[(1 - r_1)(1 - r_2)N^{\mathrm{tt}} + (r_1 - 1)r_2 N^{\mathrm{tl}} + r_1(r_2 - 1)N^{\mathrm{lt}} + r_1 r_2 N^{\mathrm{ll}}\right]
\end{aligned}
\tag{2}
$$

where

$$
\alpha = \frac{1}{(r_1 - f_1)(r_2 - f_2)}.
$$

In this expression, the subscripts refer to the $p_{\mathrm{T}}$ rank of the lepton. The $N^{\mathrm{xx}}$ are the number of events from the loose sample with leptons either passing the tight criteria (t in superscript) or passing the loose criteria but not the tight criteria (l in superscript). Care must be taken in applying the procedure to muons, since the difference between the tight and loose criteria for muons is only in the isolation requirement, and the triggers used for low-$p_{\mathrm{T}}$ muons also require isolation, meaning that $f$ for these muons is substantially higher than for muons from an unbiased trigger[4] . This is addressed by requiring low-$p_{\mathrm{T}}$ muons in the loose sample to satisfy isolation criteria similar to those applied in the trigger, and to apply different values of $r$ and $f$ for low-$p_{\mathrm{T}}$ of muons that require this isolation. A further complication may arise due to the low statistics in the loose sample, which can lead to a measured value of $N^{\mathrm{tt}}_{\mathrm{fake}}$ that is negative or very close to zero. In the case of negative values $N^{\mathrm{tt}}_{\mathrm{fake}}$ is set to zero when computing limits, and the 68% C.L. upper bound on $N^{\mathrm{tt}}_{\mathrm{fake}}$ is taken as the statistical uncertainty.

Charge misidentification is negligible for muons due to the long lever arm to the muon system and the fact that the charge is measured in both the inner detector and the muon spectrometer. For electrons, the rate of charge misidentification is calculated from a sample of $Z \to ee$ events, selected without any requirement placed on the charge of the two electron tracks. It is assumed that the rate at which the charge of an electron is misidentified varies with $\eta$ but is uncorrelated between the two electrons in each event. Further assuming that the sample consists entirely of opposite-sign electron pairs, the number of measured same-sign events where one electron is in the $i^{\mathrm{th}}$ bin of $\eta$ and the other in the $j^{\mathrm{th}}$ bin is expected to be

$$
N^{ij}_{\mathrm{ss}} \approx N^{ij}(\varepsilon_i + \varepsilon_j)
$$

where $N^{ij}$ is the total number of events in the $i$-$j$ $\eta$ bin, and $\varepsilon$ is the rate of charge mismeasurement. The value of $\varepsilon$ in each $\eta$ bin is then extracted by minimizing the Poisson likelihood for the observed number of same-sign pairs in each $\eta$ bin to be consistent with the above expectation. One limitation of this estimate is that electrons from $Z$ decay only rarely have large $p_{\mathrm{T}}$, rendering the uncertainty on the charge misidentification rate for such electrons large. To reduce this uncertainty, the rate of charge misidentification is measured using $t\bar{t}$ MC simulated events as a function of the electron $p_{\mathrm{T}}$. This rate is matched to the rate observed in data for the $p_{\mathrm{T}}$ range covered by the $Z$ events, and the rate for electrons with larger $p_{\mathrm{T}}$ is scaled according to the MC prediction. Closure tests using the $Z$ peak have been performed in data and MC simulation and show good agreement (details are provided in Fig. 19).

To determine the number of events expected from charge mismeasurement in the signal region, a sample is selected using the same criteria as for the analysis selection, except that an opposite-sign rather

[4]Electrons in principle have a similar problem, as $r$ and $f$ for electrons with $p_{\mathrm{T}} < 60$ GeV are calculated with respect to a trigger that requires isolation. However, the fact that the loose selection relaxes other selection criteria in addition to isolation lessens the importance of this bias.

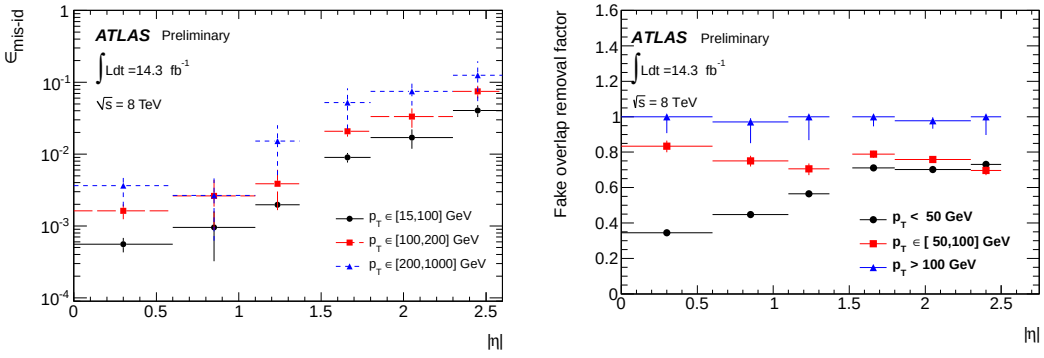


(a) (b)

Figure 2: (a) Charge misidentification rate measured in data using the likelihood method on $Z$ events, as a function of $|\eta|$ (black points). Applying the $p_T$-dependent correction factor determined with simulated $t\bar{t}$ events results in the final charge misidentification rates for higher-$p_{\mathrm{T}}$ electrons (red squares and blue triangles). (b) Correction factor applied to the charge mismeasurement rates to account for the overlap between the estimation of backgrounds from charge mismeasurement and fake electrons.

than same-sign $ee$ or $e\mu$ pair is required. The measured $\varepsilon$ values are then applied to each electron in this sample to determine the expected number of mismeasured same-sign events in the analysis sample. One source of charge mismeasurement is from "trident" electrons, where the electron emits a hard photon that subsequently produces an electron-positron pair, resulting in three tracks relatively close to each other. If the wrong track is matched to the EM cluster, the charge may be incorrect. However, such electrons will also appear to be isolated far less frequently than electrons that do not emit hard radiation will be, and therefore this source of events is also partially captured by the fake electron estimate. To correct for the overlap between the charge mismeasurement and fake electron estimates, the charge mismeasurement rate is recalculated with the estimated fake electron contribution removed from the tight selection sample. The ratio of the initial and recalculated rates is taken as an $\eta$- and $p_{\mathrm{T}}$-dependent correction factor to be applied to the charge mismeasurement rates. The measured charge mismeasurement rate and the overlap correction factor are shown in Fig. 2.

The background estimates are validated using samples selected with criteria similar to our standard selection, but where the expected yield from signal events is small. One such control region (called the $E_{\mathrm{T}}^{\mathrm{miss}}$ control region) is defined by dropping the requirement on $E_{\mathrm{T}}^{\mathrm{miss}}$ and requiring $100 < H_{\mathrm{T}} < 400$ GeV. A second region (the $H_{\mathrm{T}}$ control region) is defined by dropping the requirement on $H_{\mathrm{T}}$ and requiring $E_{\mathrm{T}}^{\mathrm{miss}} < 40$ GeV. A third region (the "zero-$b$-tag" control region) is defined by requiring all of our standard kinematic criteria but requiring that there be no $b$-tagged jets. The predicted and observed yields in the $E_{\mathrm{T}}^{\mathrm{miss}}$ control region are given in Table 2; similar agreement between the data yield and background expectation is observed in the other two control regions (details are in the appendix in Tables 15 and 16). Comparisons of kinematic distributions between the data and background model for the $E_{\mathrm{T}}^{\mathrm{miss}}$ control region are included in the appendix (Figs. 13-15).

## 5 Systematic Uncertainties

The expected signal and background yields are subject to several systematic uncertainties. For the yields derived from simulation, the largest source of uncertainty is that on the calculated cross section. For the $t\bar{t}+W/Z$ backgrounds, this is based on variations in the parton distribution functions (PDF) and renormalization and factorization scales [60], resulting in a 30% uncertainty. For other backgrounds, varying the

Table 2: Observed and expected number of events with statistical (first) and systematic (second) uncertainties for the $E_{\mathrm{T}}^{\mathrm{miss}}$ control region selection. For the Monte Carlo simulation, the systematic uncertainties include only the production cross section uncertainty.

| | Channel | | |
|---|---|---|---|
| Samples | $ee$ | $e\mu$ | $\mu\mu$ |
| Charge misidentification | $25.7 \pm 0.7 \pm 6.6$ | $30.2 \pm 0.6 \pm 7.9$ | — |
| Fakes | $38.7 \pm 3.7 \pm 11.6$ | $73.1 \pm 5.3 \pm 21.9$ | $33.4 \pm 8.5 \pm 10.0$ |
| Diboson | | | |
| • $WZ/ZZ$+jets | $3.9 \pm 0.7 \pm 1.3$ | $10.9 \pm 1.2 \pm 3.7$ | $5.1 \pm 0.8 \pm 1.7$ |
| • $W^{\pm}W^{\pm}$+2 jets | $0.4 \pm 0.2 \pm 0.2$ | $1.2 \pm 0.3 \pm 0.6$ | $0.8 \pm 0.2 \pm 0.4$ |
| $tt + W/Z$ | | | |
| • $t\bar{t}W$(+jet) | $1.7 \pm 0.1 \pm 0.5$ | $6.6 \pm 0.2 \pm 2.0$ | $4.3 \pm 0.2 \pm 1.3$ |
| • $t\bar{t}Z$(+jet) | $0.5 \pm 0.1 \pm 0.1$ | $1.5 \pm 0.1 \pm 0.5$ | $0.8 \pm 0.1 \pm 0.2$ |
| • $t\bar{t}W^{+}W^{-}$ | $0.014 \pm 0.002$ | $0.050 \pm 0.004$ | $0.029 \pm 0.003$ |
| Total expected background | $71 \pm 5 \pm 13$ | $124 \pm 8 \pm 24$ | $44 \pm 11 \pm 10$ |
| Observed | 64 | 97 | 38 |
| Signal contamination | | | |
| • $\mathrm{b}' \to Wt$ (800 GeV) | $< 0.003$ | $0.009 \pm 0.006$ | $0.002 \pm 0.001$ |
| • 4 tops contact ($C/\Lambda^2 = -4\pi$ TeV$^{-2}$) | $0.009 \pm 0.005$ | $0.06 \pm 0.02$ | $0.02 \pm 0.01$ |

renormalization and factorization scales results in uncertainties of 34% for $WZ$ and $ZZ$ production, 25% for $W^{\pm}W^{\pm}jj$ production, and +38%/-26% for $t\bar{t}W^{+}W^{-}$ production. The effect of uncertain modeling of initial- and final-state gluon radiation (ISR/FSR) is estimated by varying the parton shower parameters in PYTHIA. The uncertainty on the integrated luminosity is 3.6% [61, 62]. The largest uncertainties specific to ATLAS arise from the jet energy scale [53], the $b$-tagging efficiency [54], and the lepton identification efficiency [55–58].

Systematic uncertainties on the backgrounds estimated from data are evaluated separately. Six effects are considered when assigning the systematic uncertainty on the predicted yield of events from electron charge mismeasurement: *i*) the statistical uncertainty on the probability for an electron to have its charged mismeasured, *ii*) the statistical uncertainty on the $p_{\mathrm{T}}$-dependent correction factor, *iii*) the difference in rate obtained when applying the measurement method to simulated $Z$ boson events and the true rate observed in simulated $t\bar{t}$ events, *iv*) the difference in the $p_{\mathrm{T}}$-dependent scale factor when measured using different $t\bar{t}$ simulated samples, *v*) the variation in the result observed when the width of the $Z$ peak region is varied, and *vi*) the statistical uncertainty on the correction for the overlap in the measurement of charge misidentification and fake electron background estimates. The level of agreement between the observed and predicted yields in the control regions is taken as an estimate of the systematic uncertainty in the fake lepton prediction, resulting in a 30% uncertainty.

The sources of systematic uncertainties that contribute more than 1% uncertainty on the expected signal or background yield for the $b'$/VLQ selection are summarised in Table 3. These uncertainties have similar impact on the expected yields for the other signal models.

## 6 Selection optimisation

For each signal model, the event selection was optimised using a grid search of requirements on $H_{\mathrm{T}}$, $E_{\mathrm{T}}^{\mathrm{miss}}$, the number of jets, and the number of $b$-tagged jets. The set of criteria that provided the best expected sensitivity to new physics (including the effect of systematic uncertainties) was chosen. While

Table 3: Leading sources of systematic uncertainty on the signal and background estimates for the $b'$/VLQ selection, and their relative impact on the total background estimate. A $b'$ mass of 650 GeV is assumed.

| | Uncertainty in % | | | | | |
|---|---|---|---|---|---|---|
| | 650 GeV $b'$ | | | Background | | |
| Source | $ee$ | $e\mu$ | $\mu\mu$ | $ee$ | $e\mu$ | $\mu\mu$ |
| Cross section | – | – | – | 14.4 | 25.4 | 32.9 |
| Fakes | – | – | – | 9.7 | 1.4 | 10.1 |
| Charge misidentification | – | – | – | 7.2 | 7.1 | – |
| Jet energy scale | 4.6 | 2.5 | 0.2 | 3.5 | 10.2 | 4.4 |
| ISR/FSR | 6.0 | 6.0 | 6.0 | 2.6 | 4.5 | 4.0 |
| $b$-tagging efficiency | 4.6 | 3.1 | 3.0 | 2.1 | 4.4 | 4.0 |
| Lepton ID efficiency | 5.3 | 4.9 | 8.2 | 2.2 | 3.6 | 5.4 |
| Jet energy resolution | 0.8 | 0.9 | 0.3 | 0.9 | 2.7 | 2.0 |
| Luminosity | 3.6 | 3.6 | 3.6 | 1.6 | 2.7 | 3.6 |
| Lepton energy scale | 0.8 | 0.4 | 0.0 | 1.4 | 0.9 | 0.1 |
| JVF selection efficiency | 2.5 | 2.9 | 2.6 | 1.1 | 1.5 | 1.4 |

no improvement in the expected $b'$ mass limit is observed when requiring more than two jets, the limit does improve when stricter criteria are placed on $H_{\mathrm{T}}$, and requiring $H_{\mathrm{T}} > 650$ GeV provides the optimal selection for the $b'$ search. For the VLQ search, a similar procedure was followed, and the same conclusion was reached. Therefore the $b'$ and VLQ selections are the same.

For the four top signal, which has four $b$ jets per event, it was found that increasing the $H_{\mathrm{T}}$ requirement to 650 GeV along with requiring at least two $b$-tagged jets provided the best sensitivity. For production of two positively-charged top quarks, which has less jet activity and therefore a softer $H_{\mathrm{T}}$ distribution that the other signals, it was not found to be beneficial to tighten the $H_{\mathrm{T}}$ requirement beyond that of the base selection. However, since the $pp$ initial state of the LHC makes the $uu \to tt$ process much more common than the $\overline{uu} \to \overline{tt}$ process, both leptons are required to be positively charged for this search. A summary of the optimised selection for each channel is given in Table 4. The expected backgrounds after the optimised selection in each search are listed in Tables 5-7.

The efficiencies of the event selection for the different signals are summarised in Tables 8-11. These efficiencies include the branching fractions to two leptons of same sign, the acceptance and the selection efficiencies.

# 7 Results

The observed yields for each signal selection are given in Tables 5-7. Also, the number of observed events is compared to the expected background at each step of the selection in Table 12, with good agreement being observed. The distributions of various kinematic variables observed in data are compared to the background estimates for the $b'$/VLQ selection in Fig. 3. The $CL_s$ method [63, 64] is used to assess the consistency between the observed yields and each potential new physics signal, where the log-likelihood ratio $LLR$ is used as the test statistic. For each model, $LLR$ is defined as

$$LLR = -2 \log \frac{L_{s+b}}{L_b} \tag{3}$$

where $L_{s+b}$ ($L_b$) is the Poisson likelihood to observe the data under the signal-plus-background (background-only) hypothesis. Pseudo-experiments are generated under each hypothesis, taking into account

Table 4: Summary of the selection for the various signals. For all signals, the number of jets is required to be at least two and $E_{\mathrm{T}}^{\mathrm{miss}}$ is required to be > 40 GeV.

| Variable | $b'$ and VLQ | $tt$ | $tttt$ |
|---|---|---|---|
| $H_{\mathrm{T}}$ | > 650 GeV | > 550 GeV | > 650 GeV |
| $N_{b-jets}$ | ≥ 1 | ≥ 1 | ≥ 2 |
| Charge | ±± | ++ | ±± |

Table 5: Observed and expected number of events with statistical (first) and systematic (second) uncertainties for the $b'$/VLQ signal selection.

| Backgrounds | Channel | | |
|---|---|---|---|
| Samples | $ee$ | $e\mu$ | $\mu\mu$ |
| Charge misidentification | $0.6 \pm 0.1 \pm 0.2$ | $0.9 \pm 0.1 \pm 0.3$ | — |
| Fakes | $0.8 \pm 0.4 \pm 0.3$ | $0.2 \pm 0.4 \pm 0.1$ | $< 1.1$ |
| Diboson | | | |
| • $WZ/ZZ$+jets | $0.3 \pm 0.2 \pm 0.1$ | $0.3 \pm 0.1^{+0.4}_{-0.2}$ | $0.4 \pm 0.2 \pm 0.1$ |
| • $W^{\pm}W^{\pm}$+2 jets | $0.17 \pm 0.09 \pm 0.05$ | $0.3 \pm 0.2 \pm 0.1$ | $0.2 \pm 0.1 \pm 0.1$ |
| $t\bar{t} + W/Z$ | | | |
| • $t\bar{t}W$(+jet(s)) | $0.6 \pm 0.2 \pm 0.3$ | $1.9 \pm 0.2 \pm 0.6$ | $1.3 \pm 0.2 \pm 0.4$ |
| • $t\bar{t}Z$(+jet(s)) | $0.18 \pm 0.03 \pm 0.06$ | $0.66 \pm 0.05 \pm 0.22$ | $0.31 \pm 0.04 \pm 0.10$ |
| • $t\bar{t}W^+W^-$ | $0.024 \pm 0.003^{+0.010}_{-0.007}$ | $0.072 \pm 0.005^{+0.028}_{-0.020}$ | $0.055 \pm 0.004^{+0.022}_{-0.016}$ |
| Total expected background | $2.7 \pm 0.5 \pm 0.4$ | $4.4 \pm 0.5^{+0.9}_{-0.7}$ | $2.3 \pm 1.2 \pm 0.5$ |
| Observed | 3 | 10 | 2 |

Table 6: Observed and expected number of events with statistical (first) and systematic (second) uncertainties for the positively-charged top pair signal selection.

| | Channel | | |
|---|---|---|---|
| Samples | $ee$ | $e\mu$ | $\mu\mu$ |
| Charge misidentification | $0.6 \pm 0.1 \pm 0.2$ | $0.5 \pm 0.1 \pm 0.2$ | — |
| Fakes | $0.6 \pm 0.4 \pm 0.2$ | $1.0 \pm 0.4 \pm 0.3$ | $0.7 \pm 0.7 \pm 0.2$ |
| Diboson | | | |
| • $WZ/ZZ$+jets | $0.2 \pm 0.1 \pm 0.1$ | $0.5 \pm 0.3 \pm 0.2$ | $0.6 \pm 0.3 \pm 0.2$ |
| • $W^{\pm}W^{\pm}$+2 jets | $0.16 \pm 0.08 \pm 0.04$ | $0.3 \pm 0.2 \pm 0.1$ | $0.2 \pm 0.1 \pm 0.1$ |
| $t\bar{t} + W/Z$ | | | |
| • $t\bar{t}W$(+jet(s)) | $0.7 \pm 0.1 \pm 0.2$ | $2.2 \pm 0.1 \pm 0.7$ | $1.5 \pm 0.1 \pm 0.5$ |
| • $t\bar{t}Z$(+jet(s)) | $0.18 \pm 0.03 \pm 0.06$ | $0.59 \pm 0.05 \pm 0.19$ | $0.26 \pm 0.03 \pm 0.09$ |
| • $t\bar{t}W^+W^-$ | $0.013 \pm 0.002 \pm 0.005$ | $0.053 \pm 0.004 \pm 0.021$ | $0.032 \pm 0.003 \pm 0.013$ |
| Total | $2.5 \pm 0.4 \pm 0.4$ | $5.1 \pm 0.5 \pm 0.9$ | $3.3 \pm 0.8 \pm 0.7$ |
| Observed | 3 | 8 | 1 |

Table 7: Observed and expected number of events with statistical (first) and systematic (second) uncertainties for the four top quarks signal selection.

| | Channel | | |
|---|---|---|---|
| Samples | $ee$ | $e\mu$ | $\mu\mu$ |
| Charge misidentification | $0.16 \pm 0.04 \pm 0.05$ | $0.41 \pm 0.07 \pm 0.12$ | — |
| Fakes | $0.18 \pm 0.17 \pm 0.05$ | $0.07 \pm 0.28 \pm 0.02$ | $< 1.14$ |
| Diboson | | | |
| • $WZ/ZZ$+jets | $< 0.1$ | $0.01 \pm 0.09 \pm 0.01$ | $< 0.11$ |
| • $W^{\pm}W^{\pm}$+2 jets | $< 0.03$ | $0.18 \pm 0.16 \pm 0.07$ | $< 0.03$ |
| $t\bar{t} + W/Z$ | | | |
| • $t\bar{t}W$(+jet(s)) | $0.31 \pm 0.04 \pm 0.12$ | $0.93 \pm 0.06 \pm 0.35$ | $0.65 \pm 0.06 \pm 0.25$ |
| • $t\bar{t}Z$(+jet(s)) | $0.09 \pm 0.02 \pm 0.04$ | $0.34 \pm 0.04 \pm 0.14$ | $0.14 \pm 0.02 \pm 0.06$ |
| • $t\bar{t}W^{+}W^{-}$ | $0.012 \pm 0.002 \pm 0.005$ | $0.039 \pm 0.003 \pm 0.016$ | $0.024 \pm 0.003 \pm 0.01$ |
| Total | $0.8 \pm 0.2 \pm 0.1$ | $2.0 \pm 0.4 \pm 0.4$ | $0.8 \pm 1.2 \pm 0.3$ |
| Observed | 1 | 6 | 1 |

Table 8: Event selection efficiencies (in percent), relative to the inclusive cross section for the $b' \to Wt$ and $b' \to Wq$ ($\sim 1/3$ for each $q = u, c, t$) signals, for several generated mass points. They are computed with respect to the generated events passing the lepton filter, and where the $W$ is free to decay hadronically or leptonically.

| Process | Channel | | |
|---|---|---|---|
| | $ee$ | $e\mu$ | $\mu\mu$ |
| $b'(400\text{ GeV}) \to Wt$ | $0.11 \pm 0.01$ | $0.39 \pm 0.02$ | $0.25 \pm 0.02$ |
| $b'(600\text{ GeV}) \to Wt$ | $0.30 \pm 0.02$ | $0.82 \pm 0.03$ | $0.53 \pm 0.02$ |
| $b'(800\text{ GeV}) \to Wt$ | $0.37 \pm 0.02$ | $1.02 \pm 0.03$ | $0.64 \pm 0.02$ |
| $b'(1000\text{ GeV}) \to Wt$ | $0.35 \pm 0.02$ | $1.11 \pm 0.03$ | $0.63 \pm 0.02$ |
| $b'(400\text{ GeV}) \to Wq$ | $0.024 \pm 0.004$ | $0.082 \pm 0.007$ | $0.060 \pm 0.006$ |
| $b'(600\text{ GeV}) \to Wq$ | $0.09 \pm 0.01$ | $0.25 \pm 0.01$ | $0.14 \pm 0.01$ |
| $b'(800\text{ GeV}) \to Wq$ | $0.13 \pm 0.01$ | $0.32 \pm 0.01$ | $0.19 \pm 0.01$ |
| $b'(1000\text{ GeV}) \to Wq$ | $0.10 \pm 0.01$ | $0.32 \pm 0.02$ | $0.20 \pm 0.01$ |

Table 9: Event selection efficiencies (in percent), relative to the inclusive cross section for the vector-like $T$ ($B$) signal for several generated $T$ ($B$) mass points. Efficiencies are computed assuming the branching ratios from the singlet model.

| Process | Channel | | |
|---|---|---|---|
| | $ee$ | $e\mu$ | $\mu\mu$ |
| $TT$ (350 GeV) | $0.013 \pm 0.002$ | $0.038 \pm 0.003$ | $0.024 \pm 0.003$ |
| $TT$ (550 GeV) | $0.055 \pm 0.004$ | $0.136 \pm 0.006$ | $0.082 \pm 0.005$ |
| $TT$ (750 GeV) | $0.065 \pm 0.005$ | $0.176 \pm 0.008$ | $0.080 \pm 0.005$ |
| $TT$ (850 GeV) | $0.065 \pm 0.005$ | $0.171 \pm 0.007$ | $0.093 \pm 0.005$ |
| $BB$ (350 GeV) | $0.011 \pm 0.002$ | $0.043 \pm 0.004$ | $0.024 \pm 0.003$ |
| $BB$ (550 GeV) | $0.068 \pm 0.005$ | $0.218 \pm 0.008$ | $0.129 \pm 0.006$ |
| $BB$ (750 GeV) | $0.098 \pm 0.006$ | $0.269 \pm 0.009$ | $0.185 \pm 0.008$ |
| $BB$ (850 GeV) | $0.128 \pm 0.006$ | $0.344 \pm 0.010$ | $0.191 \pm 0.008$ |

Table 10: Event selection efficiencies (in percent), relative to the dileptonic cross section (both $W$ bosons must decay to $e$, $\mu$ or $\tau$), for the positively-charged top pair signal.

| Process | Channel | | |
|---|---|---|---|
| | $ee$ | $e\mu$ | $\mu\mu$ |
| Left-left | 0.48 ± 0.02 | 1.59 ± 0.04 | 1.27 ± 0.04 |
| Left-right | 0.41 ± 0.02 | 1.46 ± 0.04 | 1.19 ± 0.03 |
| Right-right | 0.40 ± 0.02 | 1.42 ± 0.04 | 1.14 ± 0.03 |

Table 11: Event selection efficiencies (in percent), relative to the inclusive cross section, for the four top quarks signals (all decay modes of the $W$ are included).

| Process | Channel | | |
|---|---|---|---|
| | $ee$ | $e\mu$ | $\mu\mu$ |
| Standard Model | 0.11 ± 0.01 | 0.39 ± 0.01 | 0.28 ± 0.01 |
| Contact interaction | 0.15 ± 0.01 | 0.53 ± 0.02 | 0.41 ± 0.02 |
| Sgluon (350 GeV) | 0.03 ± 0.01 | 0.09 ± 0.01 | 0.07 ± 0.01 |
| Sgluon (400 GeV) | 0.06 ± 0.01 | 0.17 ± 0.02 | 0.13 ± 0.02 |
| Sgluon (500 GeV) | 0.13 ± 0.02 | 0.47 ± 0.03 | 0.23 ± 0.02 |
| Sgluon (600 GeV) | 0.15 ± 0.02 | 0.61 ± 0.04 | 0.41 ± 0.03 |
| Sgluon (800 GeV) | 0.20 ± 0.02 | 0.75 ± 0.04 | 0.48 ± 0.03 |
| Sgluon (1000 GeV) | 0.16 ± 0.02 | 0.57 ± 0.03 | 0.49 ± 0.03 |
| 2UED/RPP (600 GeV) | 0.26 ± 0.01 | 0.93 ± 0.02 | 0.66 ± 0.02 |
| 2UED/RPP (800 GeV) | 0.25 ± 0.01 | 0.88 ± 0.02 | 0.67 ± 0.02 |
| 2UED/RPP (1000 GeV) | 0.23 ± 0.01 | 0.85 ± 0.02 | 0.67 ± 0.02 |
| 2UED/RPP (1200 GeV) | 0.22 ± 0.01 | 0.88 ± 0.02 | 0.67 ± 0.02 |

Table 12: Comparison of the number of expected background events to the number of observed events for different steps of the signal region selection. The first four selection criteria listed are used in the $b'$, VLQ, and four top quark production searches, while the final criterion is used only in the four top quark production search. The positively-charged top quark pair selection, which requires $H_T > 550$ GeV and that both leptons have positive charge, is not represented here.

| | Channel | | | | | |
|---|---|---|---|---|---|---|
| | $ee$ | | $e\mu$ | | $\mu\mu$ | |
| Selection step | Data | Backgr. | Data | Backgr. | Data | Backgr. |
| $N_{jets} \geq 2$ | 371 | 317 ± 53 | 344 | 363 ± 60 | 127 | 128 ± 24 |
| $N_{b-jets} \geq 1$ | 90 | 87 ± 16 | 139 | 154 ± 28 | 47 | 57 ± 14 |
| $E_{\mathrm{T}}^{\mathrm{miss}} > 40$ GeV | 55 | 46 ± 8 | 100 | 100 ± 17 | 37 | 40 ± 10 |
| $H_{\mathrm{T}} > 650$ GeV | 3 | 2.7 ± 0.6 | 10 | 4.4 ± 1.0 | 2 | 2.3 ± 1.2 |
| $N_{b-jets} \geq 2$ | 1 | 0.75 ± 0.25 | 6 | 2.0 ± 0.5 | 1 | 0.8 ± 1.2 |

statistical fluctuations of the total predictions according to Poisson statistics, as well as Gaussian fluctuations in the signal and background expectations describing the effect of systematic uncertainties. Signal cross sections for which $CL_s = CL_{s+b}/CL_b < 0.05$ are deemed excluded at the 95% C.L.

For each signal selection, the yield in the $ee$ and $\mu\mu$ channels is consistent with the background expectation. There is an excess of events in the $e\mu$ channel, with the excess being most significant for the four top quark production selection (see Table 7). The probability of observing six or more events, given the expected background and the statistical and systematic uncertainties on that expectation, is 3.9%. Since this probability is not small enough to support any claim of new physics, we interpret the data as constraining each of the new physics models, and report the 95% C.L. limits (upper limits for cross sections, or lower limits for masses) relevant for each model.

For the $b'$ and VLQ selection, 15 events are observed with $9.26 \pm 0.78$ expected from background. This observation places 95% C.L. upper limits on the $b'$ pair production cross section, as shown in Fig. 4. Comparison with the calculated cross section implies that the mass of the $b'$ must be $> 0.72$ TeV, assuming 100% branching fraction to $Wt$. The corresponding expected lower limit in the absence of a signal contribution is 0.77 TeV, and the observed result is consistent with this expectation at about the one standard deviation level. If light quark decays are also considered, the limits become weaker due to the lower efficiency for events with one or zero $b$ jets to satisfy our selection criteria. A two-dimensional scan of excluded $b'$ masses as a function of branching fraction to $Wt$ is shown in Fig. 5. The full branching ratio plane is not excluded for any mass point, since as the BR($b' \to Wt$) goes to zero, no same-sign dileptons and b-jets are produced.

Limits on the VLQ pair-production cross section, assuming the branching fractions to $W$, $Z$, and $H$ modes prescribed by the singlet model, are shown in Fig. 6. Comparison with the calculated cross section results in lower limits on the $B$ mass of 0.59 TeV and on the $T$ mass of 0.54 TeV at 95% C.L. The expected limits in the absence of a signal contribution are 0.63 TeV for the $B$ mass and 0.59 TeV for the $T$ mass. If the three branching fractions are allowed to vary independently, the data can be interpreted as excluding at 95% C.L. some of the possible sets of branching ratios for a given $B$ or $T$ mass. These exclusions are shown in Figs. 7 and 8.

For the positively-charged top quark pair selection, 12 events are observed with $10.9 \pm 1.6$ expected from background. This implies upper limits on the production cross section of 0.19 pb for left-left chirality, 0.20 pb for left-right chirality, and 0.21 pb for right-right chirality, as shown in Table 13. The corresponding expected limits in the absence of a signal contribution are $0.19^{+0.09}_{-0.05}$ pb, $0.21^{+0.09}_{-0.06}$ pb, and $0.22^{+0.10}_{-0.07}$ pb, respectively. For each chirality, the upper limit on $C$ as a function of $\Lambda$ is shown in Figure 9.

For the four top selection, 8 events are observed with $3.6 \pm 1.3$ expected from background. This translates to an upper limit on the cross section of 85 fb assuming SM kinematics, or to a limit of 59 fb for production with a new-physics contact interaction. Both of these results are consistent with the expected limits within one standard deviation, as shown in Table 14. In the context of specific new physics models, we find that the lower limit on the sgluon mass is 0.80 TeV, assuming that the gluons are pair-produced and always decay to $t\bar{t}$ (for an expected limit of 0.83 TeV); the lower-limit on the Kaluza-Klein mass is 0.90 TeV (for an expected limit of 0.92 TeV); and, in the contact interaction model, the upper limit on $C$ depends on the value of $\Lambda$, as shown in Fig. 10.

# 8 Conclusion

A search for new physics has been performed using events with two leptons of the same electric charge, at least one identified $b$ jet, sizable missing transverse momentum, and large $H_{\mathrm{T}}$. Several new physics effects could enhance the yield of such events over the small SM expectation. The search has been done in the context of several new physics models, with event selection criteria optimised for each scenario. No significant excess of events over background is observed for any of the selections, resulting in the 95%

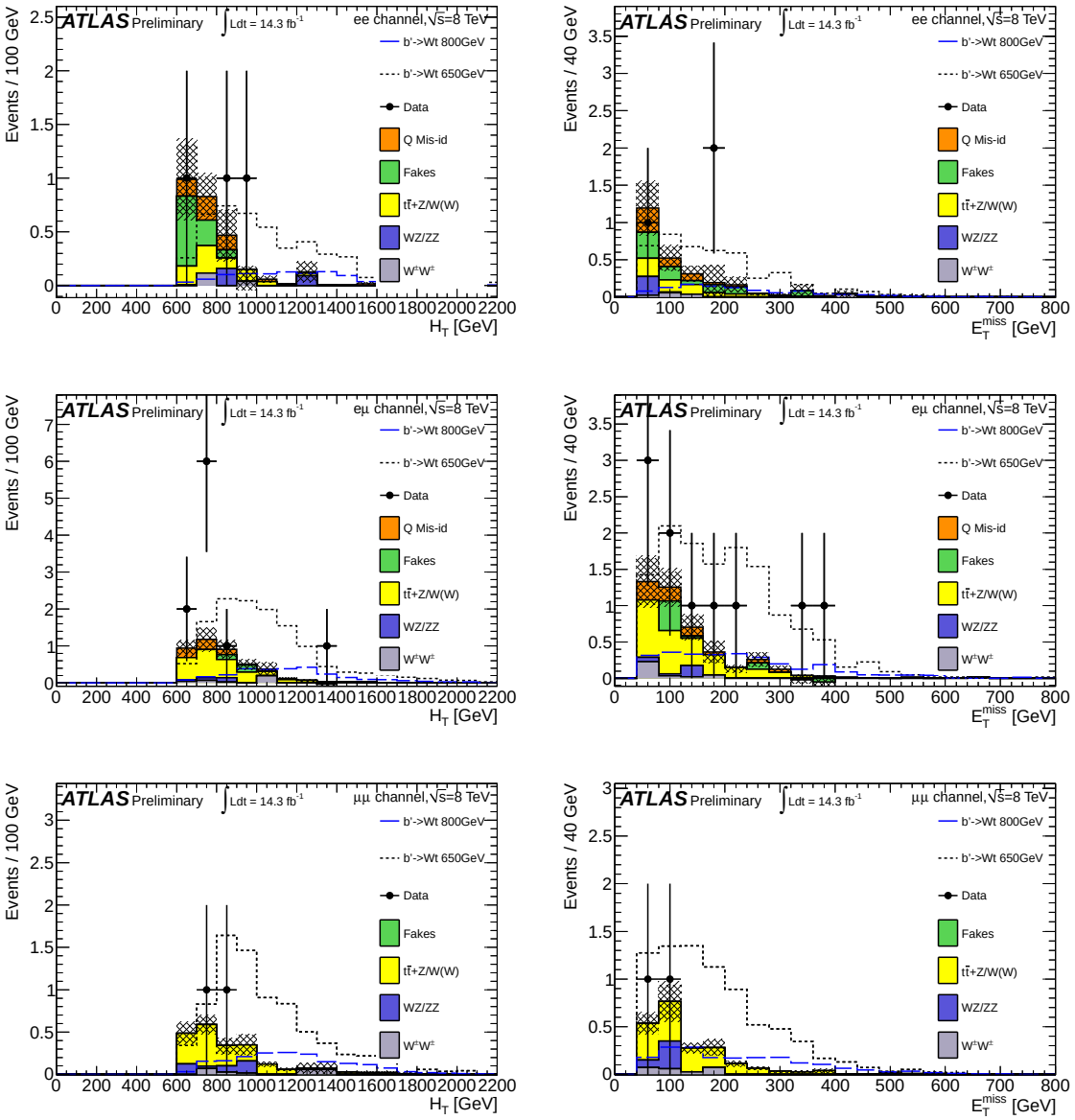


Figure 3: Distribution of kinematic variables for the data (points) and for the estimated background (histograms), after applying the $b'$/VLQ signal selection. The shaded areas correspond to the total uncertainties on the background, where statistical uncertainties are dominant. For the Monte Carlo simulated samples, systematic uncertainties include only the production cross section uncertainties.

Table 13: Expected and observed limits on the positively-charged top quark pair production signal.

| | 95% C.L. upper limit | | |
|---|---|---|---|
| | $\sigma(pp \to tt)$ [pb] | | $\lvert C\rvert/\Lambda^2$ [TeV$^{-2}$] |
| Chirality configuration | Expected 1$\sigma$ range | Observed | Observed |
| Left-left | 0.14-0.28 | 0.19 | 0.092 |
| Left-right | 0.15-0.30 | 0.20 | 0.271 |
| Right-right | 0.15-0.32 | 0.21 | 0.099 |

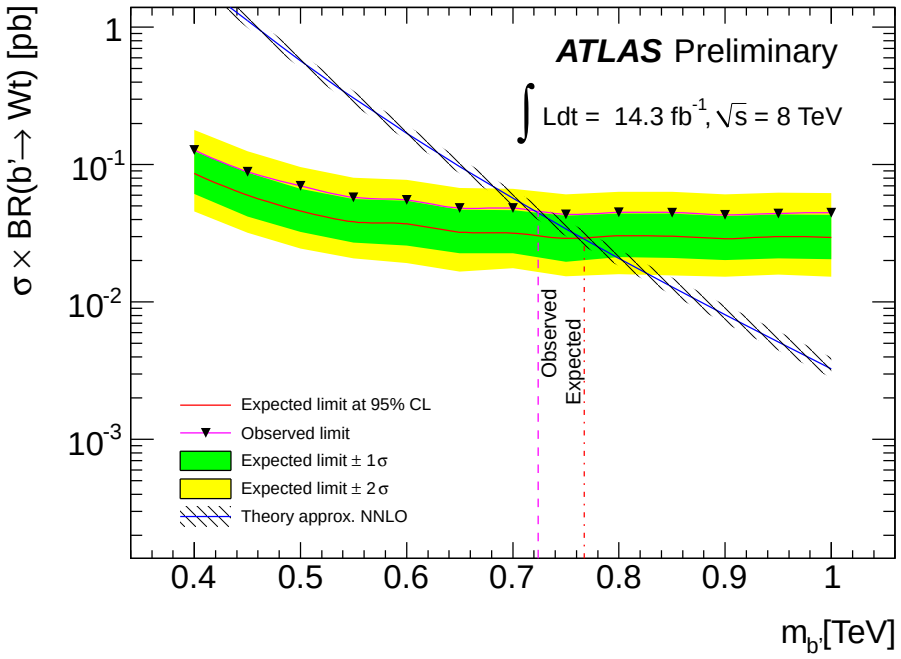


Figure 4: Expected and observed upper limits on the pair production cross section of $b' \to Wt$, as a function of the $b'$ mass.

Table 14: Expected and observed limits on two four top quarks signals.

| | 95% C.L. upper limit | | |
|---|---|---|---|
| | $\sigma(pp \to t\bar{t}t\bar{t})$ [fb] | | $\lvert C\rvert/\Lambda^2$ [TeV$^{-2}$] |
| Model | Expected 1$\sigma$ range | Observed | Observed |
| Standard Model | 43-89 | 85 | — |
| Contact interaction | 29-61 | 59 | 15 |

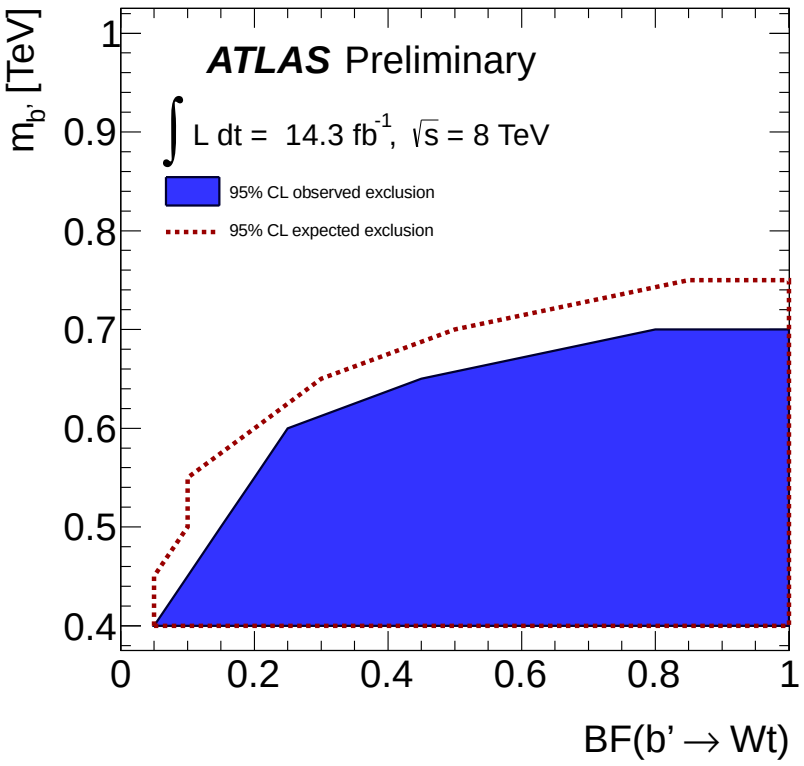


Figure 5: Expected and observed upper limit contours on the pair production cross section of $b' \to Wq$, as a function of the $b'$ mass and the branching ratio to $Wt$, calculated from the $b' \to Wq$ sample. The MC simulated signal samples used in this plot are statistically independent of those used to produce the 1D limits (Fig. 4), leading to a slight difference in the mass limit for BR($b' \to Wt$) = 100%.

C.L. limits $m_{b'} > 0.72$ TeV (assuming 100% branching fraction to $Wt$), $m_B > 0.59$ TeV, $m_T > 0.54$ TeV (assuming branching fractions to the $W$, $Z$, and $H$ decay modes arising from a singlet model), cross section for production of two positively-charged top quarks < 0.21 pb, SM four top production cross section < 85 fb, sgluon mass > 0.80 TeV and Kaluza-Klein mass (in the context of models with two universal extra dimensions) > 0.90 TeV.

## References


[1] ATLAS Collaboration, *Observation of a new particle in the search for the Standard Model Higgs boson with the ATLAS detector at the LHC*, Phys.Lett. **B716** (2012) 1–29, arXiv:1207.7214 [hep-ex].

[2] CMS Collaboration, *Observation of a new boson at a mass of 125 GeV with the CMS experiment at the LHC*, Physics Letters B **716** (2012) 30 – 61.

[3] S. Bar-Shalom, M. Geller, S. Nandi, and A. Soni, *Two Higgs doublets, a 4th generation and a 125 GeV Higgs*, arXiv:1208.3195 [hep-ph].

[4] B. A. Dobrescu and C. T. Hill, *Electroweak symmetry breaking via top condensation seesaw*, Phys.Rev.Lett. **81** (1998) 2634–2637, arXiv:hep-ph/9712319 [hep-ph].

[5] R. S. Chivukula, B. A. Dobrescu, H. Georgi, and C. T. Hill, *Top quark seesaw theory of electroweak symmetry breaking*, Phys.Rev. **D59** (1999) 075003, arXiv:hep-ph/9809470 [hep-ph].

[6] H.-J. He, C. T. Hill, and T. M. Tait, *Top quark seesaw, vacuum structure and electroweak precision constraints*, Phys.Rev. **D65** (2002) 055006, arXiv:hep-ph/0108041 [hep-ph].

[7] C. T. Hill and E. H. Simmons, *Strong dynamics and electroweak symmetry breaking*, Phys.Rept. **381** (2003) 235–402, arXiv:hep-ph/0203079 [hep-ph].

[8] R. Contino, L. Da Rold, and A. Pomarol, *Light custodians in natural composite Higgs models*, Phys.Rev. **D75** (2007) 055014, arXiv:hep-ph/0612048 [hep-ph].

[9] C. Anastasiou, E. Furlan, and J. Santiago, *Realistic Composite Higgs Models*, Phys.Rev. **D79** (2009) 075003, arXiv:0901.2117 [hep-ph].

[10] K. Kong, M. McCaskey, and G. W. Wilson, *Multi-lepton signals from the top-prime quark at the LHC*, JHEP **1204** (2012) 079, arXiv:1112.3041 [hep-ph].

[11] A. Carmona, M. Chala, and J. Santiago, *New Higgs Production Mechanism in Composite Higgs Models*, JHEP **1207** (2012) 049, arXiv:1205.2378 [hep-ph].

[12] M. Gillioz, R. Grober, C. Grojean, M. Muhlleitner, and E. Salvioni, *Higgs Low-Energy Theorem (and its corrections) in Composite Models*, JHEP **1210** (2012) 004, arXiv:1206.7120 [hep-ph].

[13] A. Davidson and K. C. Wali, *Family mass hierarchy from universal seesaw mechanism*, Phys. Rev. Lett. **60** (1988) 1813–1816.

[14] K. S. Babu and R. N. Mohapatra, *Solution to the strong* CP *problem without an axion*, Phys. Rev. D **41** (1990) 1286–1291.

[15] B. Grinstein, M. Redi, and G. Villadoro, *Low Scale Flavor Gauge Symmetries*, JHEP **1011** (2010) 067, arXiv:1009.2049 [hep-ph].

[16] D. Guadagnoli, R. N. Mohapatra, and I. Sung, *Gauged Flavor Group with Left-Right Symmetry*, JHEP **1104** (2011) 093, arXiv:1103.4170 [hep-ph].

[17] N. Arkani-Hamed, A. Cohen, E. Katz, and A. Nelson, *The Littlest Higgs*, JHEP **0207** (2002) 034, arXiv:hep-ph/0206021 [hep-ph].

[18] T. Han, H. E. Logan, B. McElrath, and L.-T. Wang, *Phenomenology of the little Higgs model*, Phys.Rev. **D67** (2003) 095004, arXiv:hep-ph/0301040 [hep-ph].

[19] M. Perelstein, M. E. Peskin, and A. Pierce, *Top quarks and electroweak symmetry breaking in little Higgs models*, Phys.Rev. **D69** (2004) 075002, arXiv:hep-ph/0310039 [hep-ph].

[20] M. Schmaltz and D. Tucker-Smith, *Little Higgs review*, Ann.Rev.Nucl.Part.Sci. **55** (2005) 229–270, arXiv:hep-ph/0502182 [hep-ph].

[21] M. S. Carena, J. Hubisz, M. Perelstein, and P. Verdier, *Collider signature of T-quarks*, Phys.Rev. **D75** (2007) 091701, arXiv:hep-ph/0610156 [hep-ph].

[22] S. Matsumoto, T. Moroi, and K. Tobe, *Testing the Littlest Higgs Model with T-parity at the Large Hadron Collider*, Phys.Rev. **D78** (2008) 055018, arXiv:0806.3837 [hep-ph].

[23] J. Aguilar-Saavedra, *Effects of mixing with quark singlets*, Phys.Rev. **D67** (2003) 035003, arXiv:hep-ph/0210112 [hep-ph].

[24] Y. Okada and L. Panizza, *LHC signatures of vector-like quarks*, arXiv:1207.5607 [hep-ph].

[25] J. Aguilar-Saavedra, *Identifying top partners at LHC*, JHEP **0911** (2009) 030, arXiv:0907.3155 [hep-ph].

[26] M. Aliev, H. Lacker, U. Langenfeld, S. Moch, P. Uwer, et al., *HATHOR: HAdronic Top and Heavy quarks crOss section calculatoR*, arXiv:1007.1327 [hep-ph].

[27] V. Barger, A. L. Stange, and R. J. N. Phillips, *Four-heavy-quark hadroproduction*, Phys. Rev. D **44** (1991) 1987–1996.

[28] V. Barger, W.-Y. Keung, and B. Yencho, *Triple-Top Signal of New Physics at the LHC*, Phys.Lett. **B687** (2010) 70–74, arXiv:1001.0221 [hep-ph].

[29] C. Degrande, J.-M. Gerard, C. Grojean, F. Maltoni, and G. Servant, *Non-resonant New Physics in Top Pair Production at Hadron Colliders*, JHEP **1103** (2011) 125, arXiv:1010.6304 [hep-ph].

[30] T. Plehn and T. M. Tait, *Seeking Sgluons*, J.Phys. **G36** (2009) 075001, arXiv:0810.3919 [hep-ph].

[31] S. Choi, M. Drees, J. Kalinowski, J. Kim, E. Popenda, et al., *Color-Octet Scalars of N=2 Supersymmetry at the LHC*, Phys.Lett. **B672** (2009) 246–252, arXiv:0812.3586 [hep-ph].

[32] C. Kilic, T. Okui, and R. Sundrum, *Vectorlike Confinement at the LHC*, JHEP **1002** (2010) 018, arXiv:0906.0577 [hep-ph].

[33] C. Kilic, T. Okui, and R. Sundrum, *Colored Resonances at the Tevatron: Phenomenology and Discovery Potential in Multijets*, JHEP **0807** (2008) 038, arXiv:0802.2568 [hep-ph].

[34] G. Burdman, B. A. Dobrescu, and E. Ponton, *Resonances from two universal extra dimensions*, Phys.Rev. **D74** (2006) 075008, arXiv:hep-ph/0601186 [hep-ph].

[35] S. Calvet, B. Fuks, P. Gris, and L. Valery, *Searching for sgluons in multitop events at a center-of-mass energy of 8 TeV*, JHEP **1304** (2013) 043, arXiv:1212.3360 [hep-ph].

[36] D. Goncalves-Netto, D. Lopez-Val, K. Mawatari, T. Plehn, and I. Wigmore, *Sgluon Pair Production to Next-to-Leading Order*, Phys.Rev. **D85** (2012) 114024, arXiv:1203.6358 [hep-ph].

[37] G. Cacciapaglia, A. Deandrea, and J. Llodra-Perez, *A Dark Matter candidate from Lorentz Invariance in* 6*D*, JHEP **1003** (2010) 083. [arXiv:0907.4993v1 [hep-ph]].

[38] A. Arbey, G. Cacciapaglia, A. Deandrea, and B. Kubik, *Dark Matter in a twisted bottle*, JHEP **1301** (2013) 147. [arXiv:1210.0384v1 [hep-ph]].

[39] ATLAS Collaboration, *Search for exotic same-sign dilepton signatures (b' quark, $T_{5/3}$ and four top quarks production) in 4.7fb$^{-1}$ of pp collisions at $\sqrt{s}$ = 7 TeV with the ATLAS detector*, ATLAS-CONF-2012-130 (2012) .

[40] J. Aguilar-Saavedra and M. Perez-Victoria, *No like-sign tops at Tevatron: Constraints on extended models and implications for the t tbar asymmetry*, Phys.Lett. **B701** (2011) 93–100, arXiv:1104.1385 [hep-ph].

[41] E. L. Berger, Q.-H. Cao, C.-R. Chen, C. S. Li, and H. Zhang, *Top Quark Forward-Backward Asymmetry and Same-Sign Top Quark Pairs*, Phys.Rev.Lett. **106** (2011) 201801, arXiv:1101.5625 [hep-ph].

[42] ATLAS Collaboration, *Search for same-sign top-quark production and fourth-generation down-type quarks in pp collisions at $\sqrt{s}$ = 7 TeV with the ATLAS detector*, JHEP **1204** (2012) 069, arXiv:1202.5520 [hep-ex].

[43] CMS Collaboration, *Search for T5/3 top partners in same-sign dilepton final state*, CMS-PAS-B2G-12-012 (2013) .

[44] ATLAS Collaboration, *The ATLAS Experiment at the CERN Large Hadron Collider*, JINST **3** (2008) S08003.

[45] T. Sjostrand and S. Mrenna and P.Z. Skands, *PYTHIA 6.4 Physics and Manual*, JHEP **05** (2006) 026, hep-ph/0603175.

[46] J. Alwall, M. Herquet, F. Maltoni, O. Mattelaer, and T. Stelzer, *MadGraph 5 : Going Beyond*, JHEP **1106** (2011) 128, arXiv:1106.0522 [hep-ph].

[47] T. Gleisberg et al., *Event generation with SHERPA 1.1*, JHEP **0902** (2009) 007.

[48] S. Agostinelli et al., *Geant4 A Simulation Toolkit*, Nucl. Instr. and Meth. **A506** (2003) 250.

[49] ATLAS Collaboration, *The ATLAS Simulation Infrastructure*, Eur. Phys. J. **C70** (2010) 823–874, arXiv:1005.4568 [physics.ins-det].

[50] M. Cacciari, G. P. Salam, and G. Soyez, *The Anti-k(t) jet clustering algorithm*, JHEP **0804** (2008) 063, arXiv:0802.1189 [hep-ph].

[51] M. Cacciari and G. P. Salam, *Dispelling the N3 myth for the kt jet-finder*, Physics Letters B **641** (2006) 57 – 61.

[52] M. Cacciari, G. P. Salam, and G. Soyez, *FastJet User Manual*, Eur.Phys.J. **C72** (2012) 1896, arXiv:1111.6097 [hep-ph].

[53] ATLAS Collaboration, G. Aad et al., *Jet energy measurement with the ATLAS detector in proton-proton collisions at* $\sqrt{s} = 7$ *TeV*, Eur.Phys.J. **C73** (2013) 2304, arXiv:1112.6426 [hep-ex].

[54] ATLAS Collaboration, *Commissioning of the ATLAS high-performance b-tagging algorithms in the 7 TeV collision data*, ATLAS-CONF-2011-102, ATLAS-COM-CONF-2011-110.

[55] ATLAS Collaboration, *Electron performance measurements with the ATLAS detector using the 2010 LHC proton-proton collision data*, Eur. Phys. J. **C72** (2012) 1909, arXiv:1110.3174 [hep-ex].

[56] ATLAS Collaboration, *Muon reconstruction efficiency in reprocessed 2010 LHC proton-proton collision data recorded with the ATLAS detector*, ATLAS-CONF-2011-063 (2011) . https://cdsweb.cern.ch/record/1345743.

[57] ATLAS Collaboration, *A measurement of the muon reconstruction efficiency in 2010 ATLAS data using jpsi decays*, ATLAS-CONF-2012-125. https://cds.cern.ch/record/1474642.

[58] ATLAS Collaboration, *Muon Momentum Resolution in First Pass Reconstruction of pp Collision Data Recorded by ATLAS in 2010*, ATLAS-CONF-2011-046. https://cdsweb.cern.ch/record/1338575.

[59] K. Rehermann and B. Tweedie, *Efficient Identification of Boosted Semileptonic Top Quarks at the LHC*, JHEP **1103** (2011) 059, arXiv:1007.2221 [hep-ph].

[60] J. M. Campbell and R. K. Ellis, $t\bar{t}W^{+-}$ *production and decay at NLO*, JHEP **1207** (2012) 052, arXiv:1204.5678 [hep-ph].

[61] ATLAS Collaboration, *Luminosity Determination in pp Collisions at* $\sqrt{s} = 7$ TeV *Using the ATLAS Detector at the LHC*, Eur. Phys. J. **C71** (2011) 1630, arXiv:1101.2185 [hep-ex].

[62] ATLAS Collaboration, *Luminosity Determination in pp Collisions at* $\sqrt{s} = 7$ TeV *using the ATLAS Detector in 2011*, ATLAS-CONF-2011-116 (2011) . https://cdsweb.cern.ch/record/1376384.

[63] T. Junk, *Confidence level computation for combining searches with small statistics*, Nucl.Instrum.Meth. **A434** (1999) 435–443, arXiv:hep-ex/9902006 [hep-ex].

[64] A. L. Read, *Presentation of search results: the CL s technique*, Journal of Physics G: Nuclear and Particle Physics **2810** (2002) 2693. http://stacks.iop.org/0954-3899/28/i=10/a=313.

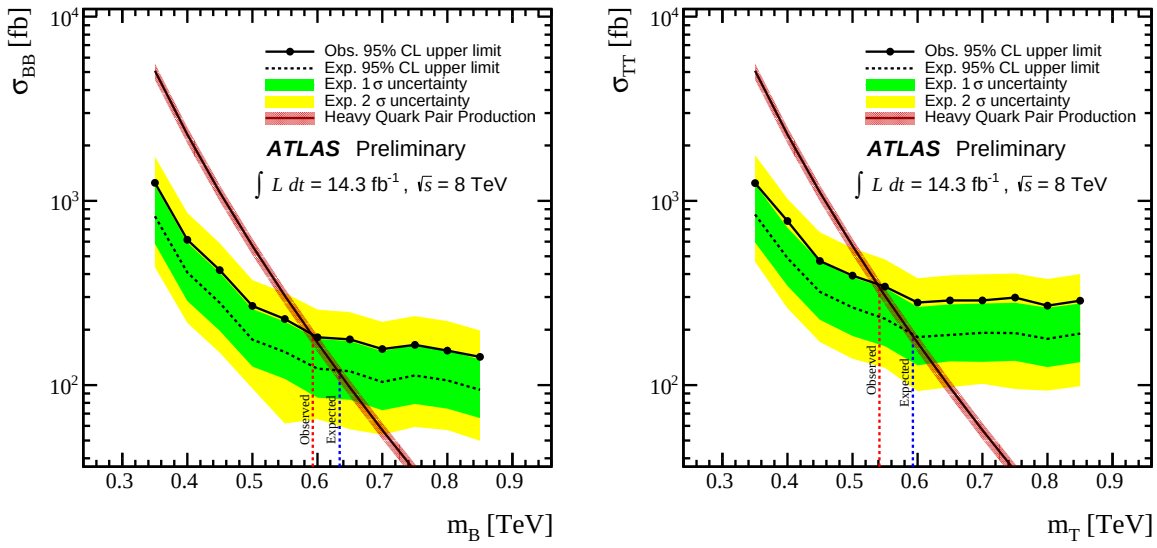


(a) (b)

Figure 6: Observed limits on the mass of (a) vector-like $B$ and (b) vector-like $T$ quarks. These limits assume pair production, with branching ratios given by model where the $B$ and $T$ quarks exist as singlets [25].

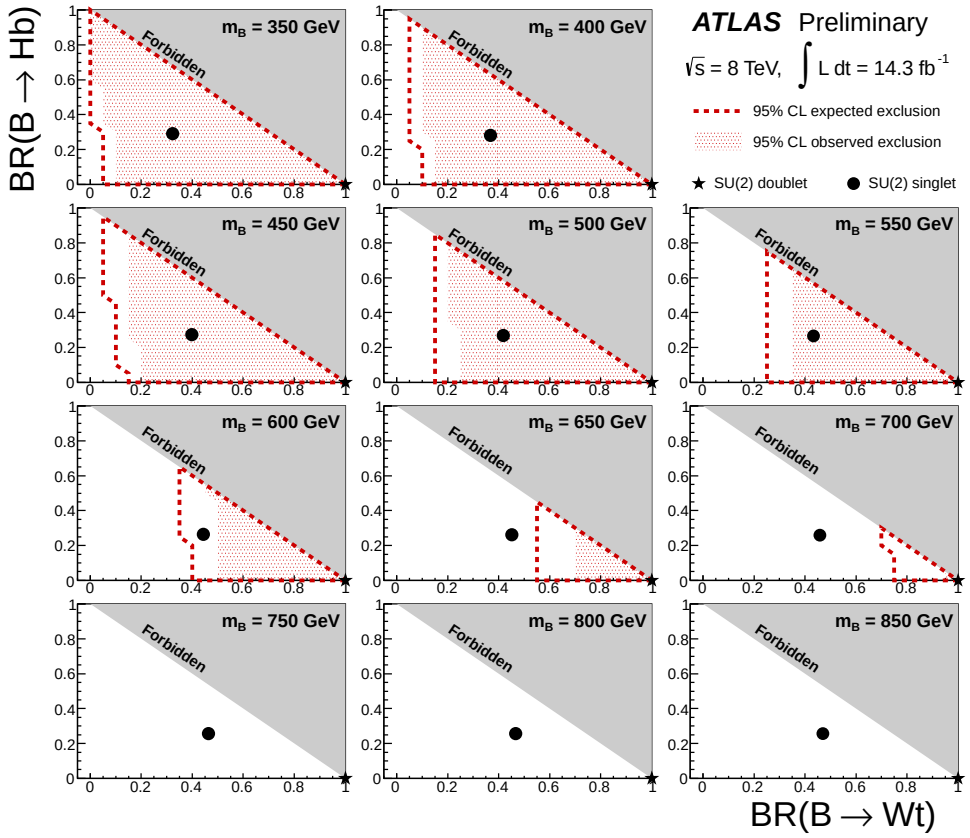


Figure 7: Observed and expected vector-like $B$ quark branching fractions excluded at 95% C.L. for several $B$ quark mass hypotheses. For reference, the branching fractions expected in models [25] where the $B$ quark is in a SU(2) singlet (doublet) are indicated by a circle (star).

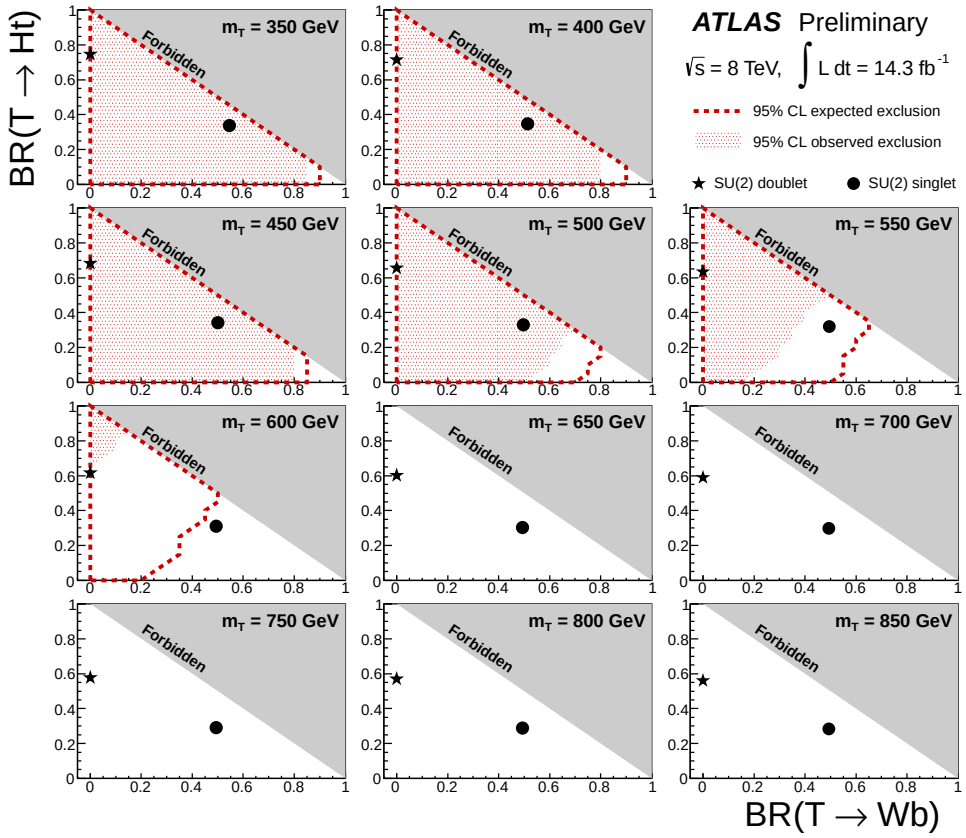


Figure 8: Observed and expected vector-like $T$ quark branching fractions excluded at 95% C.L. for several $T$ quark mass hypotheses. For reference, the branching fractions expected in models [25] where the $T$ quark is in a SU(2) singlet (doublet) are indicated by a circle (star).

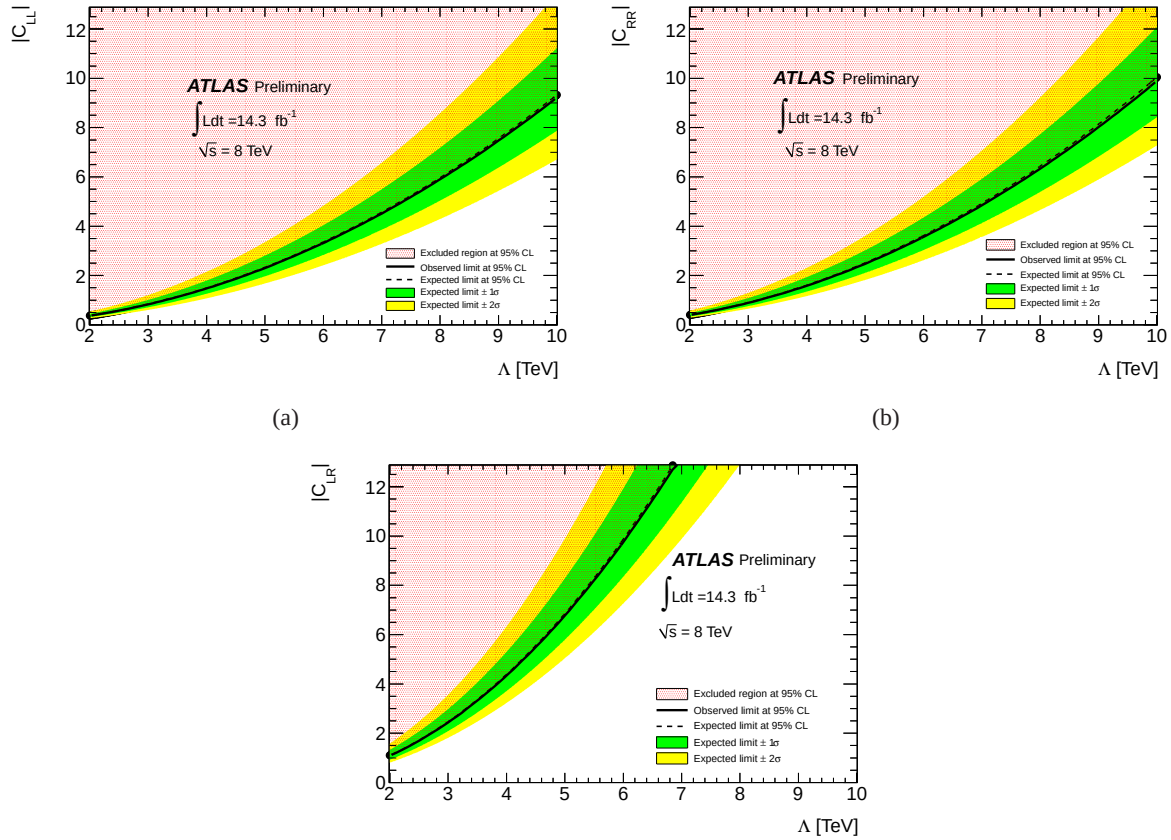


Figure 9: Observed limits on positively-charged top quark pair production in the plane of the coupling constant $C$ as a function of the new physics energy scale $\Lambda$ (as defined in Eq. 9.1 of [42]) for (a) left-left, (b) right-right, and (c) left-right chiralities. The hashed region is excluded at 95% C.L..

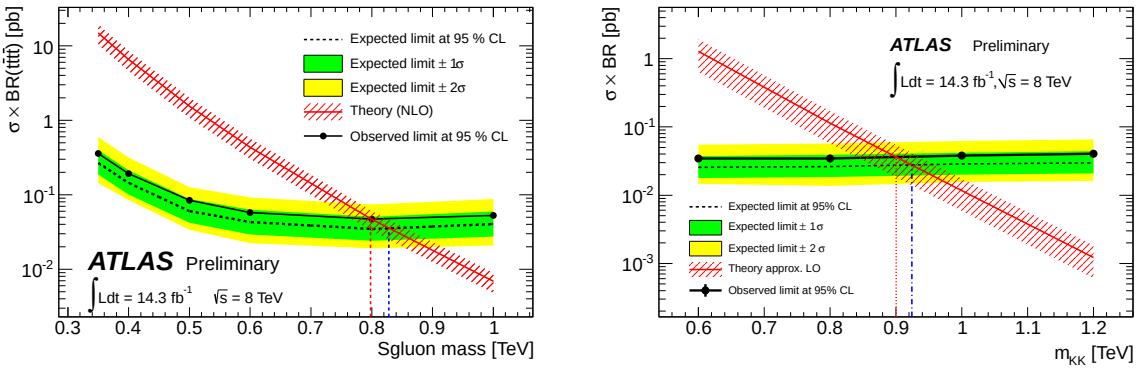


(a) (b)

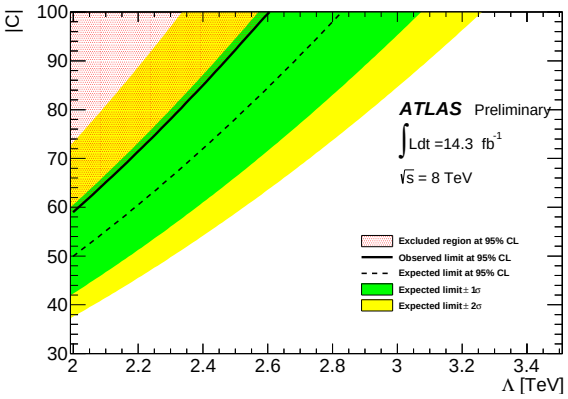


(c)

Figure 10: Observed limits on the four top quarks events production interpreted in the context of (a) sgluon pair production, (b) the 2UED/RPP model, and (c) the four-fermion contact interaction of Eq. 1 (in (c) the hashed region is excluded at 95% C.L.).

# A Additional plots and tables

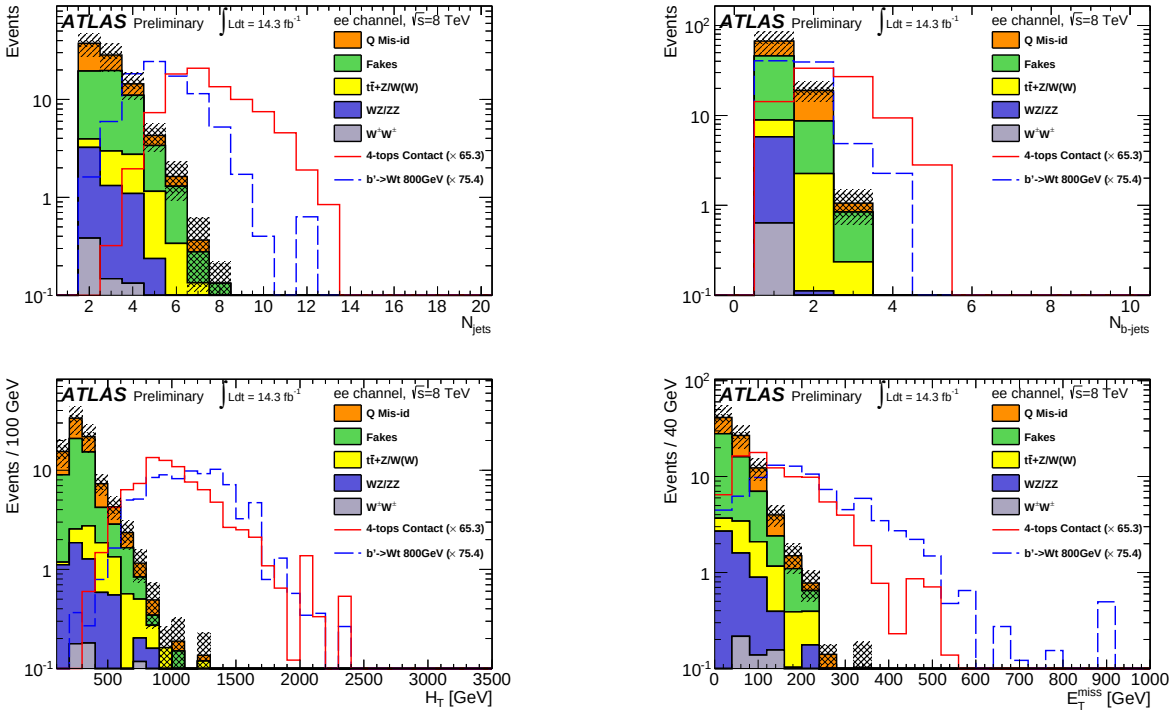


Figure 11: Distributions of discriminant variables in the *ee* channel, after the standard object selection and with the requirement that $E_{\mathrm{T}}^{\mathrm{miss}} > 40$ GeV. The cross section for each signal model is scaled up so that the signal integrals are all equal to the background integral. The assumed strength of the contact interaction is $C/\Lambda^2 = -4\pi\ \mathrm{TeV}^{-2}$. The background histograms are stacked to show the total expected background, while each signal histogram is independent of the others. The uncertainties on the background shown here consist of the production cross section uncertainty for the backgrounds modelled with Monte Carlo simulation, and a 30% uncertainty for instrumental backgrounds (see Section 5).

Table 15: Observed and expected number of events with statistical (first) and systematic (second) uncertainties for the $H_{\mathrm{T}}$ control region selection. For the Monte Carlo samples, the systematic uncertainties include only the production cross section uncertainty.

| | Channel | | |
|---|---|---|---|
| Samples | $ee$ | $e\mu$ | $\mu\mu$ |
| Charge misidentification | $13.3 \pm 0.5 \pm 3.5$ | $9.3 \pm 0.4 \pm 2.5$ | — |
| Fakes | $24.3 \pm 3.3 \pm 7.3$ | $34.0 \pm 3.9 \pm 10.2$ | $11.7 \pm 6.9 \pm 3.5$ |
| Diboson | | | |
| • $WZ/ZZ$+jets | $2.6 \pm 0.6 \pm 0.9$ | $7.1 \pm 1.0 \pm 2.4$ | $2.4 \pm 0.6 \pm 0.8$ |
| • $W^{\pm}W^{\pm}$+2 jets | $0.09 \pm 0.06 \pm 0.05$ | $0.7 \pm 0.2 \pm 0.4$ | $0.4 \pm 0.1 \pm 0.2$ |
| $t\bar{t} + W/Z$ | | | |
| • $t\bar{t}W$(+jet) | $0.6 \pm 0.1 \pm 0.2$ | $2.5 \pm 0.1 \pm 0.8$ | $1.6 \pm 0.1 \pm 0.5$ |
| • $t\bar{t}Z$(+jet) | $0.38 \pm 0.04 \pm 0.11$ | $1.0 \pm 0.1 \pm 0.3$ | $0.5 \pm 0.1 \pm 0.2$ |
| • $t\bar{t}W^{+}W^{-}$ | $0.007 \pm 0.001$ | $0.034 \pm 0.003$ | $0.021 \pm 0.003$ |
| Total | $41 \pm 5 \pm 8$ | $55 \pm 6 \pm 11$ | $17 \pm 9 \pm 4$ |
| Observed | 35 | 39 | 10 |
| Signal contamination | | | |
| • $b' \to Wt$ (800 GeV) | $0.03 \pm 0.01$ | $0.13 \pm 0.02$ | $0.09 \pm 0.02$ |
| • 4 tops contact ($C/\Lambda^2 = -4\pi$ TeV$^{-2}$) | $0.10 \pm 0.03$ | $0.34 \pm 0.05$ | $0.41 \pm 0.05$ |

Table 16: Observed and expected number of events with statistical (first) and systematic (second) uncertainties for the zero-$b$-tag control region selection. For the Monte Carlo samples, the systematic uncertainties include only the production cross section uncertainty.

| | Channel | | |
|---|---|---|---|
| Samples | $ee$ | $e\mu$ | $\mu\mu$ |
| Charge misidentification | $99.1 \pm 1.6 \pm 26.3$ | $12.0 \pm 0.4 \pm 3.2$ | — |
| Fakes | $80.2 \pm 8.0 \pm 24.1$ | $80.7 \pm 6.1 \pm 24.2$ | $21.3 \pm 4.0 \pm 6.4$ |
| Diboson | | | |
| • $WZ/ZZ$+jets | $40.5 \pm 2.1 \pm 13.8$ | $89.9 \pm 3.0 \pm 30.5$ | $36.7 \pm 2.0 \pm 12.5$ |
| • $W^{\pm}W^{\pm}$+2 jets | $6.0 \pm 0.5 \pm 3.0$ | $22.0 \pm 1.0 \pm 11.0$ | $12.0 \pm 0.8 \pm 6.0$ |
| $t\bar{t} + W/Z$ | | | |
| • $t\bar{t}W$(+jet) | $0.9 \pm 0.1 \pm 0.3$ | $2.9 \pm 0.1 \pm 0.9$ | $2.0 \pm 0.1 \pm 0.6$ |
| • $t\bar{t}Z$(+jet) | $0.29 \pm 0.04 \pm 0.09$ | $0.99 \pm 0.07 \pm 0.30$ | $0.50 \pm 0.06 \pm 0.15$ |
| • $t\bar{t}W^{+}W^{-}$ | $0.021 \pm 0.003$ | $0.053 \pm 0.004$ | $0.039 \pm 0.004$ |
| Total | $227 \pm 12 \pm 38$ | $208 \pm 11 \pm 41$ | $73 \pm 8 \pm 15$ |
| Observed | 281 | 205 | 80 |
| Signal contamination | | | |
| • $b' \to Wt$ (800 GeV) | $0.25 \pm 0.04$ | $0.53 \pm 0.06$ | $0.49 \pm 0.05$ |
| • 4 tops contact ($C/\Lambda^2 = -4\pi$ TeV$^{-2}$) | $0.06 \pm 0.02$ | $0.17 \pm 0.04$ | $0.12 \pm 0.03$ |

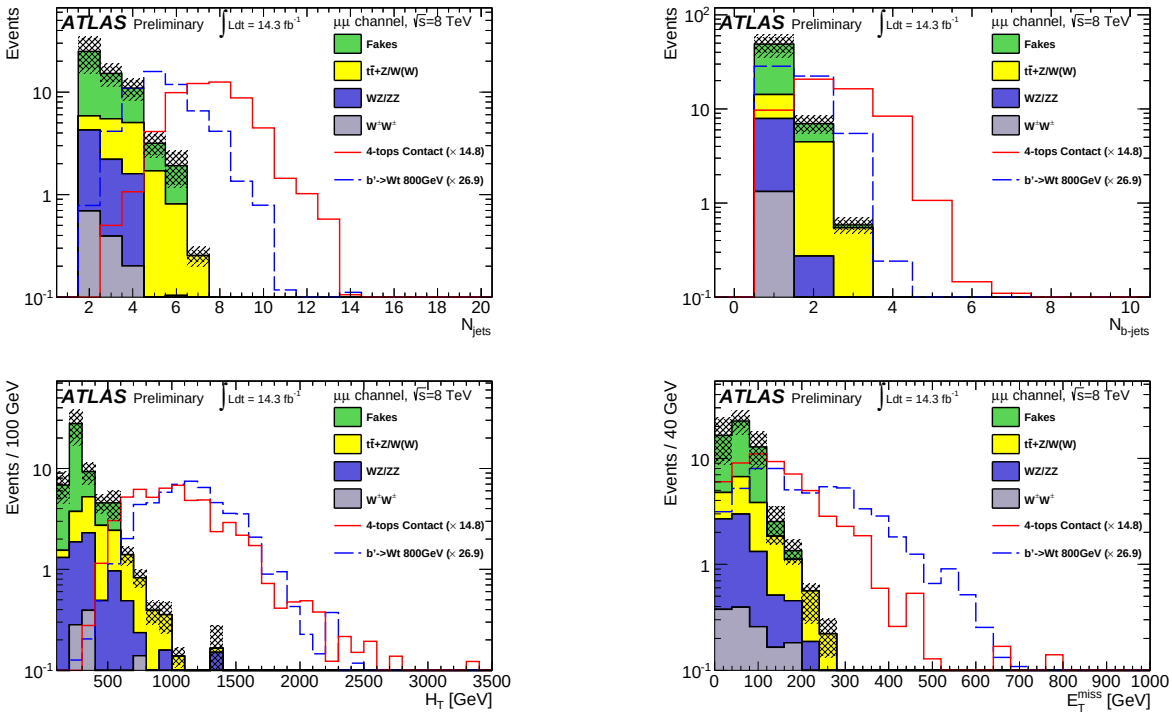


Figure 12: Distributions of discriminant variables in the $\mu\mu$ channel, after the standard object selection and with the requirement that $E_{\mathrm{T}}^{\mathrm{miss}} > 40$ GeV. The cross section for each signal model is scaled up so that the signal integrals are all equal to the total background integral. The assumed strength of the contact interaction is $C/\Lambda^2 = -4\pi\,\mathrm{TeV}^{-2}$. The background histograms are stacked to show the total expected background, while each signal histogram is independent of the others. The uncertainties on the background shown here consist of the production cross section uncertainty for the backgrounds modelled with Monte Carlo simulation, and a 30% uncertainty for instrumental backgrounds (see Section 5).

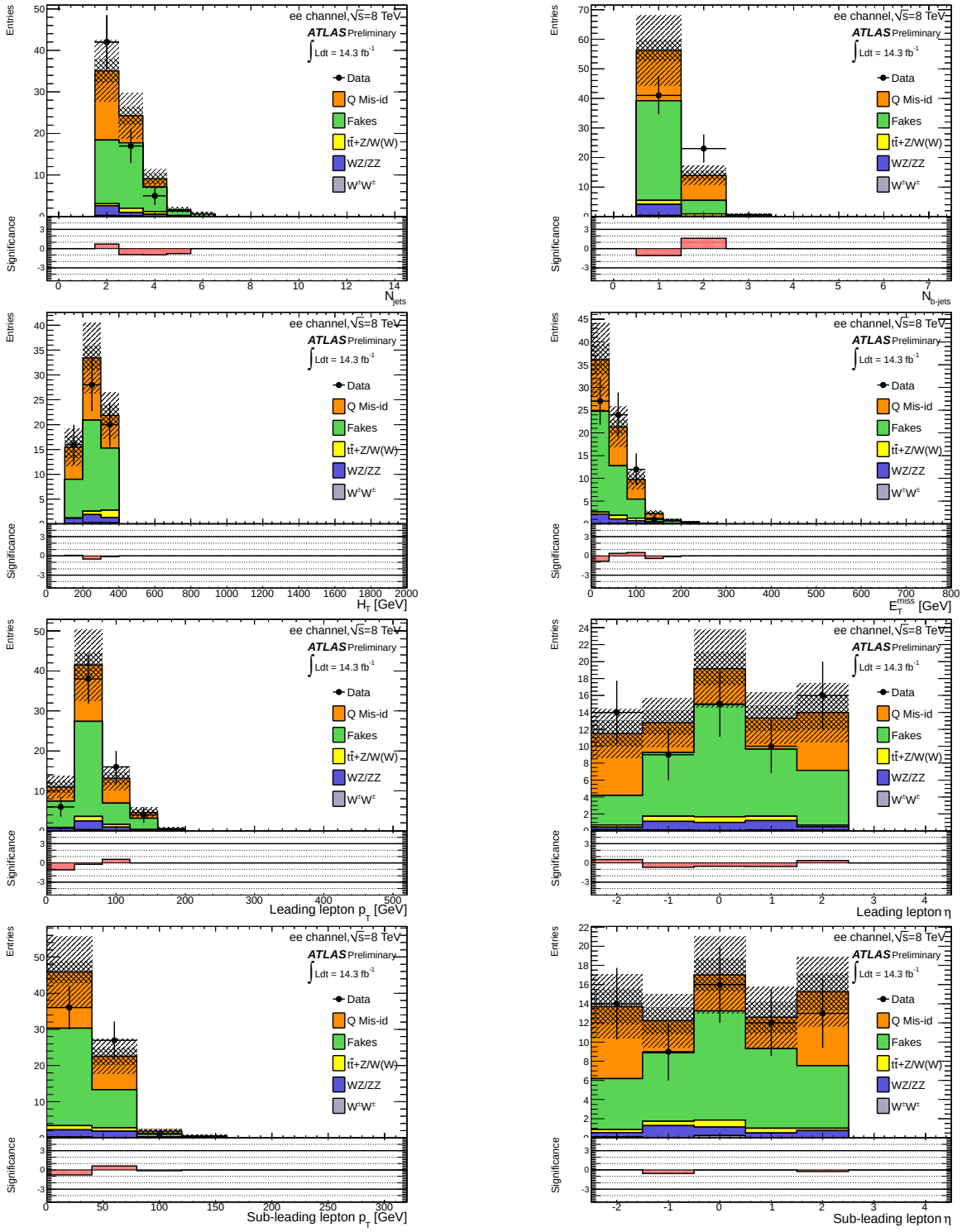


Figure 13: Distributions of some kinematic variables in the *ee* channel, after the $E_{\mathrm{T}}^{\mathrm{miss}}$ control region selection, for both the background estimation and the data. The bottom plots show the significance of the measured number of events in the data over the estimated number of events from the backgrounds.

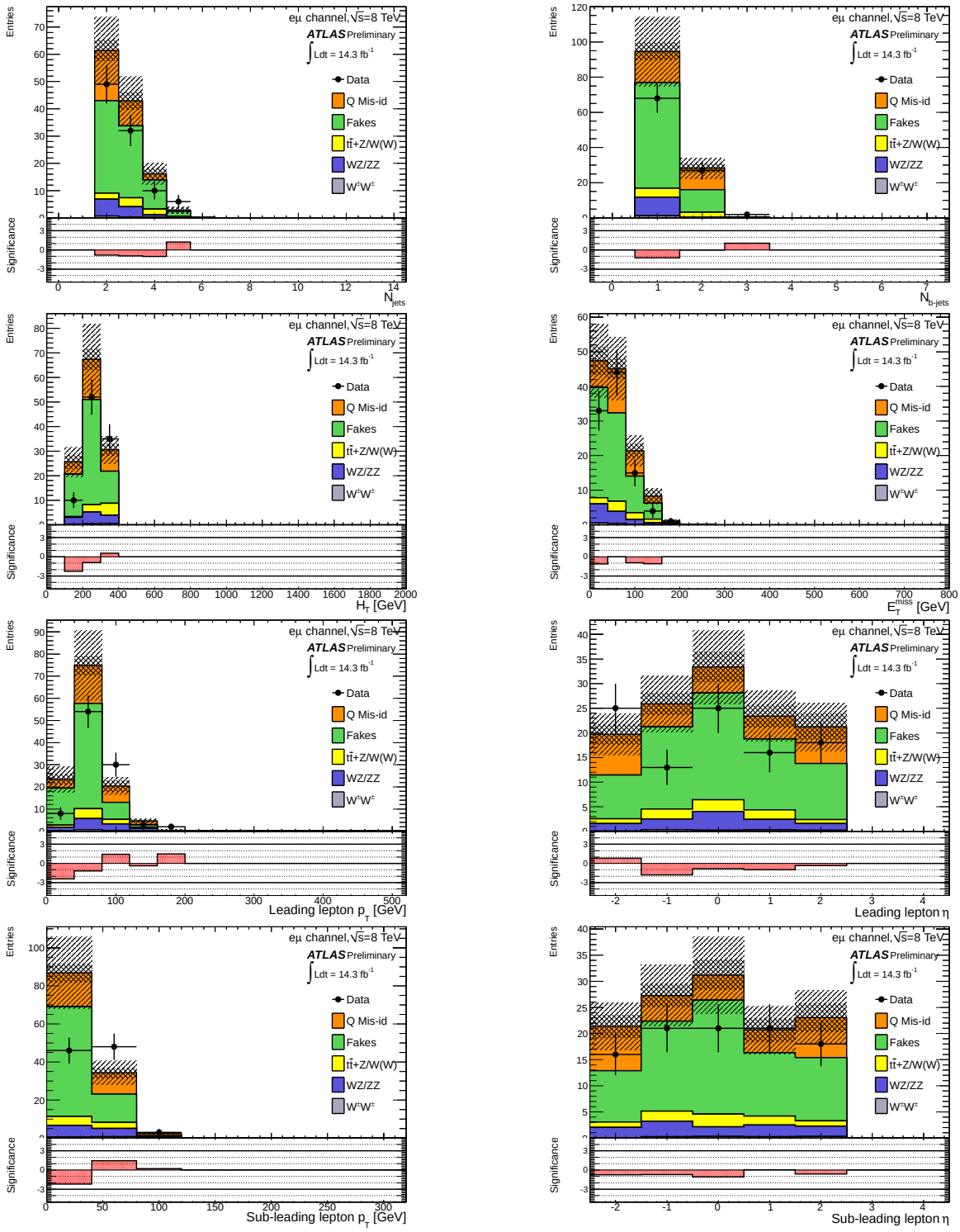


Figure 14: Distributions of some kinematic variables in the $e\mu$ channel, after the $E_{\mathrm{T}}^{\mathrm{miss}}$ control region selection, for both the background estimation and the data. The bottom plots show the significance of the measured number of events in the data over the estimated number of events from the backgrounds.

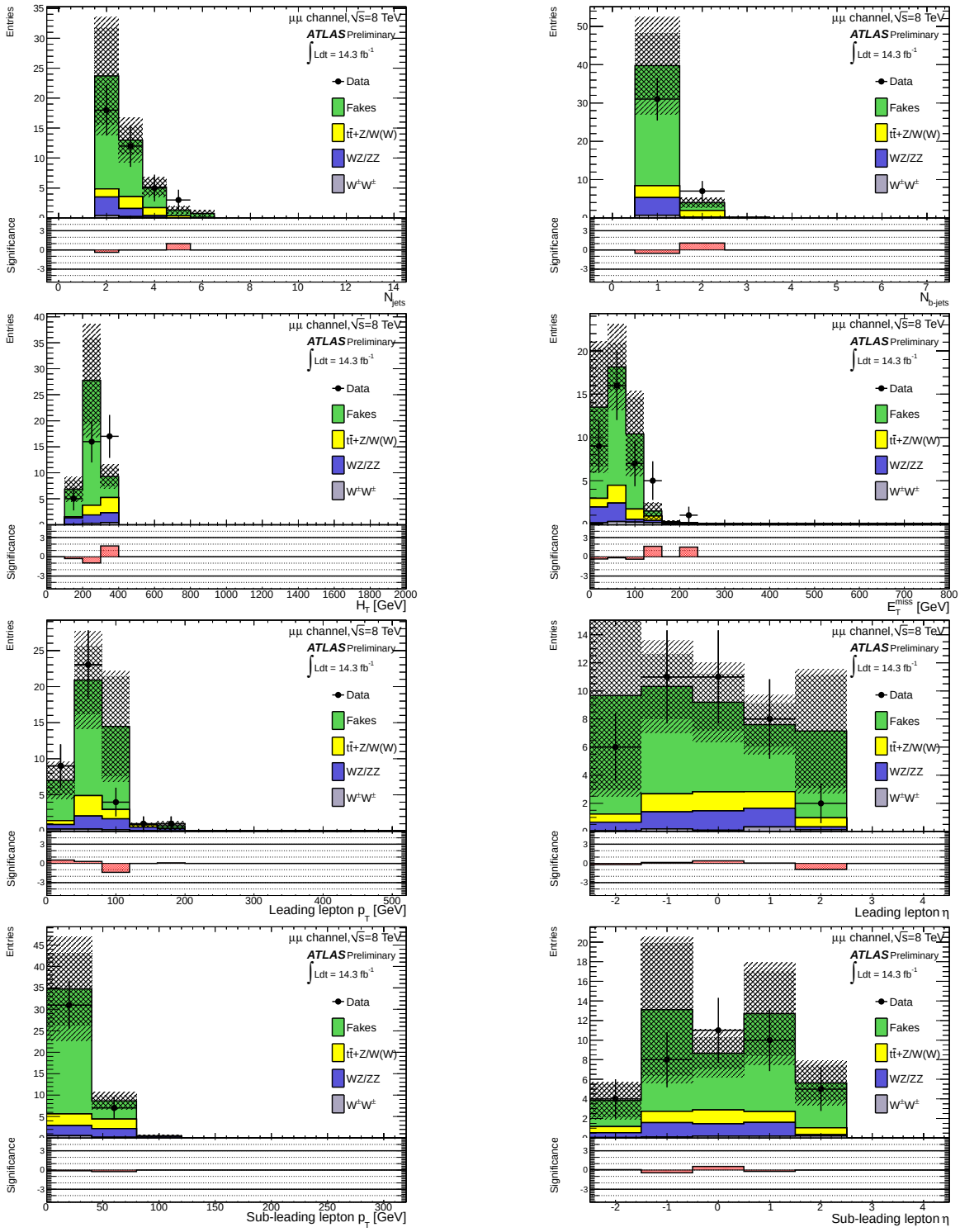


Figure 15: Distributions of some kinematic variables in the $\mu\mu$ channel, after the $E_{\mathrm{T}}^{\mathrm{miss}}$ control region selection, for both the background estimation and the data. The bottom plots show the significance of the measured number of events in the data over the estimated number of events from the backgrounds.

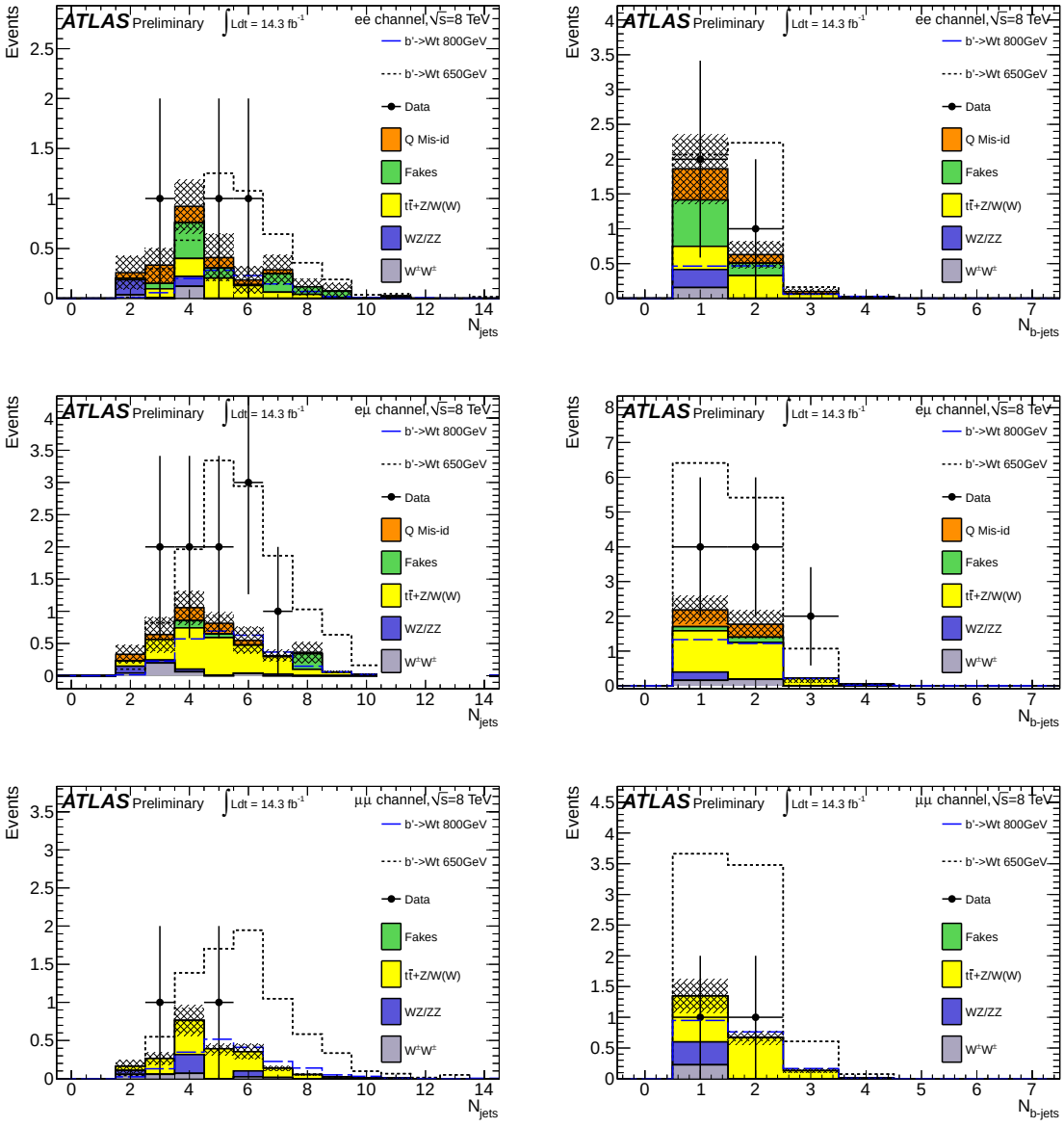


Figure 16: Distribution of kinematic variables for the data (points) and for the estimated background (histograms), after applying the $b'$/VLQ signal selection. The shaded areas correspond to the total uncertainties on the background, where statistical uncertainties are dominant. For the Monte Carlo simulated samples, systematic uncertainties include only the production cross section uncertainties.

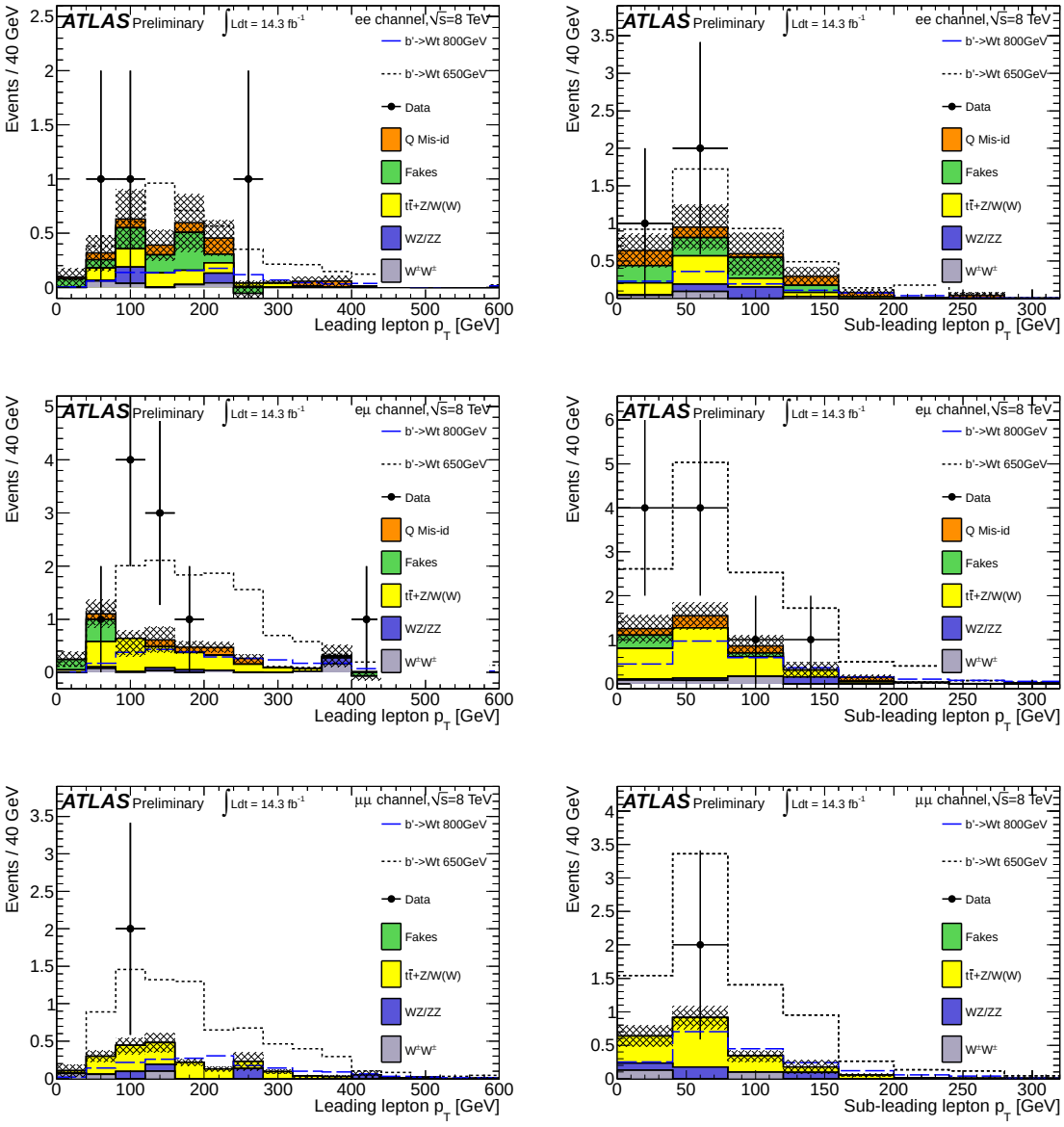


Figure 17: Distribution of kinematic variables for the data (points) and for the estimated background (histograms), after applying the $b'$/VLQ signal selection. The shaded areas correspond to the total uncertainties on the background, where statistical uncertainties are dominant. For the Monte Carlo simulated samples, systematic uncertainties include only the production cross section uncertainties.

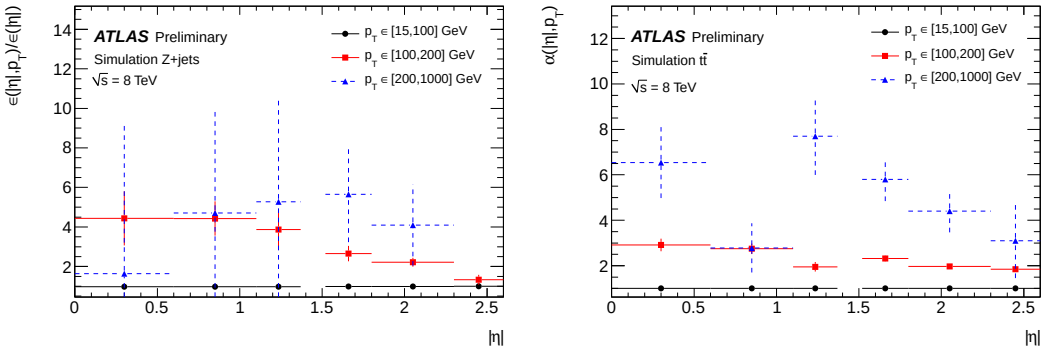


(a) (b)

Figure 18: The charge misidentification rates shown in Fig. 2(a) have been computed using the likelihood method after correction. They are defined as $\epsilon(|\eta|, p_T) = \epsilon(|\eta|) \times \alpha(|\eta|, p_T)$ where $\epsilon(|\eta|)$ corresponds to the misidentification rates measured in data on $Z$ events using the likelihood without correction, and $\alpha(|\eta|, p_T)$ is the $p_T$ dependent correction factor extracted from a $t\bar{t}$ sample. The reason for which the rates $\epsilon(|\eta|)$ need to be corrected is that they are applied to events mostly coming from $t\bar{t}$: the misidentification rates also depend on the electron $p_T$, but the $p_T$ spectrum of the electrons coming from a $Z$ decay is not the same as the one in the $t\bar{t}$. The left plot (a) shows the distribution of the ratio $\epsilon(|\eta|, p_T)/\epsilon(|\eta|)$ for $Z$ MC events computed by truth-matching as a function of $|\eta|$ and for different $p_T$ bins. It shows that the average rate $\epsilon(|\eta|)$ is largely dominated by the first bin in $p_T$. The right plot (b) shows the $p_T$ dependent correction factor $\alpha(|\eta|, p_T) = \epsilon(|\eta|, p_T)/\epsilon(|\eta|, p_T < 100\text{GeV})$ extracted from $t\bar{t}$ events computed by truth-matching, as a function of $|\eta|$ and for different $p_T$ bins. By definition, the correction factor is 1 in the first $p_T$ bin.

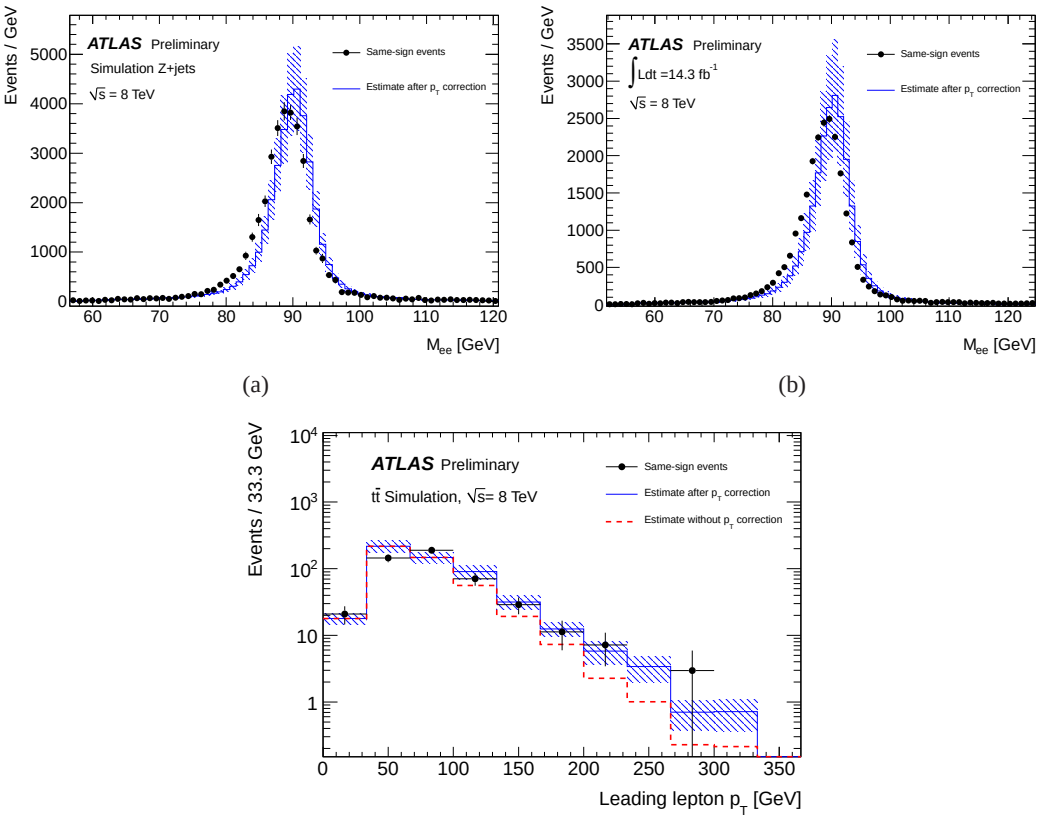


Figure 19: One way to validate the misidentification rate measurement method is via the closure test, where the number of measured same-sign events is compared with respect to the estimated number of same-sign events. This last one is computed by reweighing the measured number of opposite-sign events. This comparison was done using simulated $Z \rightarrow e^+e^-$ samples and using data. In simulated $Z$ samples (a), the number of same-sign $Z$ events is $32995 \pm 790$, while the estimation is $32493^{+6394}_{-6306}$. In data (b), the number of same-sign $Z$ events is 22067 for an estimate of $21824^{+5678}_{-5706}$. In both cases, the uncertainties combine the statistical and systematic uncertainties. A last validation of the method can be done by applying the misidentification rates measured using simulated $Z$ events after $p_T$ correction to simulated opposite-sign $t\bar{t}$ events and compare to the number of simulated same-sign $t\bar{t}$ events. The distribution of the leading electron $p_T$ can be seen in (c) and shows very good agreement within uncertainties: above 100 GeV, the total number of same-sign events is $121 \pm 19$, for an estimate of $146 \pm 36$ after the $p_T$ correction. The distribution of the leading electron $p_T$ before the $p_T$ dependent correction is also shown in (c).

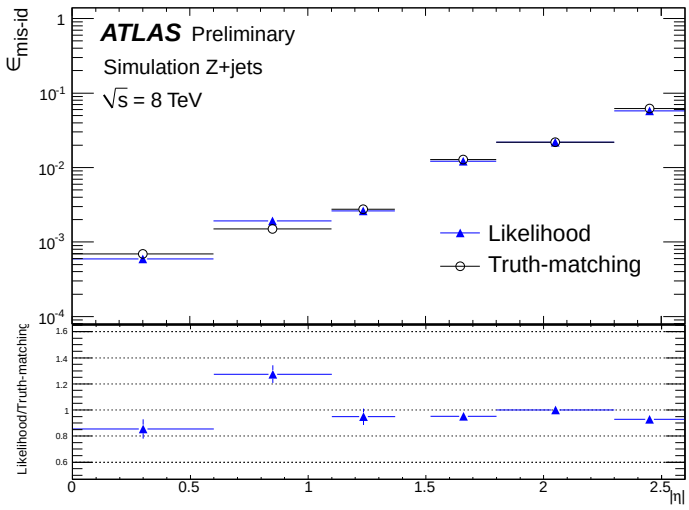


Figure 20: The likelihood method used to compute the misidentification rates as a function of $|\eta|$ can be validated using simulated $Z \rightarrow e^+e^-$ samples. The validation is done by comparing the rates extracted with the likelihood method with respect to the rates computed using the truth-matching method. As shown in the bottom plot, the likelihood measured rates are compatible with the true rates within uncertainties.

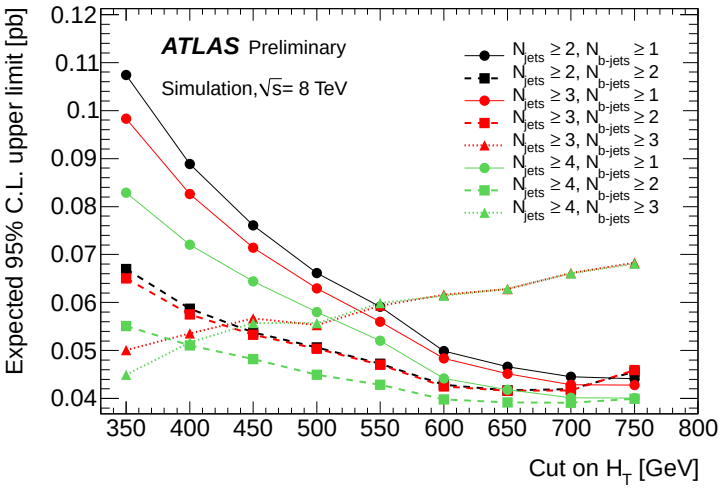


Figure 21: Expected 95% C.L. upper limit on the four tops contact interaction production cross section as a function of the cut on $H_T$, and parametrized with the requirement on the number of jets (different colors), and on the number of $b$-jets (different markers). The final event selection is chosen so that it can provide the minimum value on the cross-section. Following the information provided by this plot, the best choice for the final selection is $H_T \geq 650$ GeV, $N_{jets} \geq 2$ and $N_{b-jets} \geq 2$.

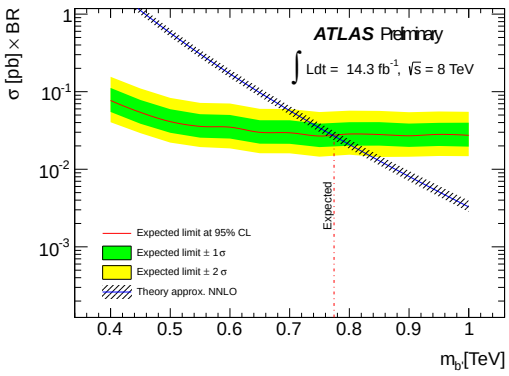


Figure 22: Expected limit on the $b'$ pair-production cross section as a function of the $b'$ mass assuming statistical uncertainties only.

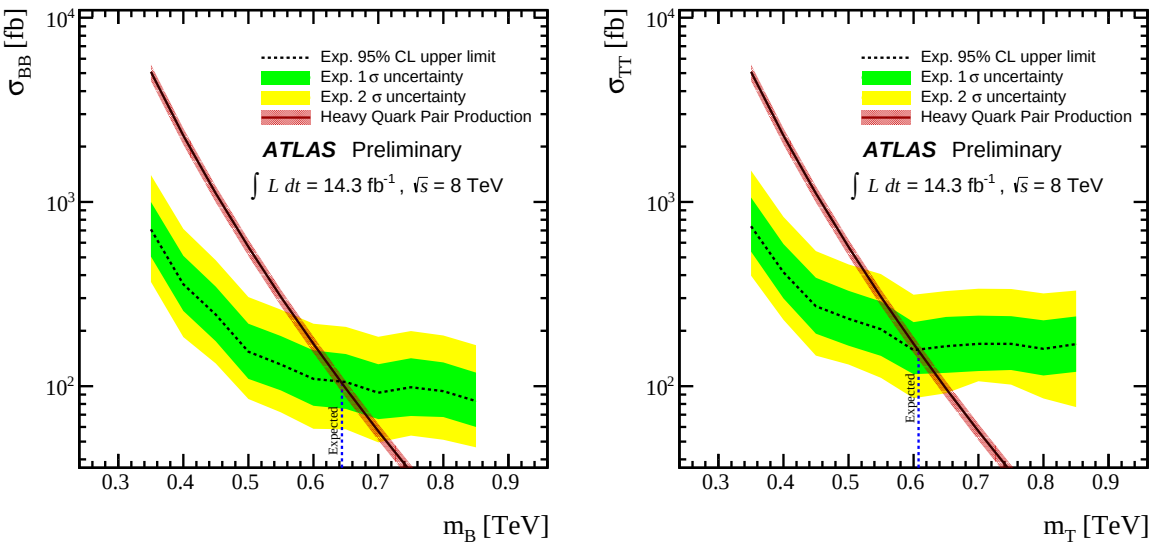


Figure 23: Expected limits on the production cross section of a vector like quark pair, as a function of the quark mass, with statistical uncertainties only for bottom like quarks (left) and top like quarks (right).

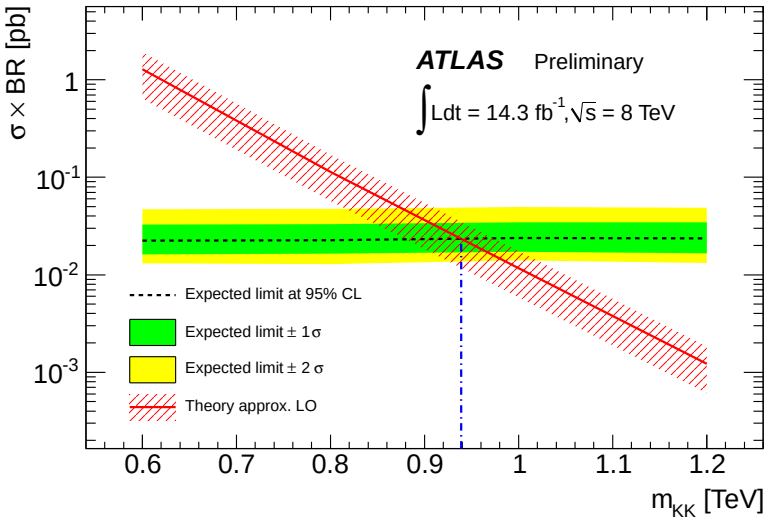


Figure 24: Expected limits on the production cross section of four top quarks events from the 2UED/RPP model, with only statistical uncertainties considered.

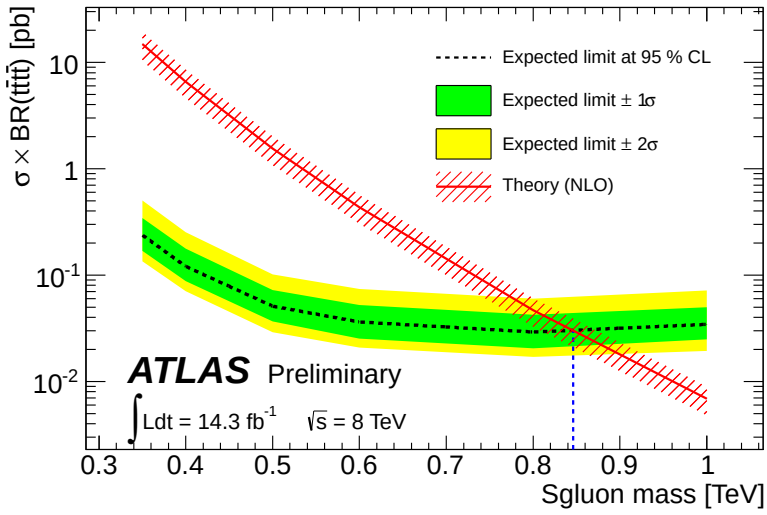


Figure 25: Expected limit on the sgluon pair-production cross section as a function of the sgluon mass assuming statistical uncertainties only.